

# Effects of streamwise elongated and spanwise periodic surface roughness elements on boundary-layer instability

Csaba B. Kátai<sup>†</sup> and Xuesong Wu

Department of Mathematics, Imperial College London, 180 Queen's Gate, London SW7 2AZ, UK

(Received xx; revised xx; accepted xx)

1 We investigate the impact on the boundary-layer stability of spanwise periodic, stream-  
 2 wise elongated surface roughness elements. Our interest is in their effects on the so-  
 3 called lower-branch Tollmien–Schlichting modes, and so the spanwise spacing of the  
 4 elements is taken to be comparable with the spanwise wavelength of the latter, which  
 5 is of  $O(R^{-3/8}L)$ , where  $L$  is the dimensional length from the leading edge of the  
 6 flat plate to the surface roughness, and  $R$  is the Reynolds number based on  $L$ . The  
 7 streamwise length is much longer, consistent with experimental setup. The roughness  
 8 height is chosen such that the wall shear is altered by  $O(1)$ . From the generic triple-  
 9 deck theory for three-dimensional roughness elements with both the streamwise and  
 10 spanwise length scales being of  $O(R^{-3/8}L)$ , we derived the relevant governing equations  
 11 by appropriate rescaling. The resulting equations are nonlinear but parabolic because the  
 12 pressure gradient in the streamwise direction is negligible while in the spanwise direction  
 13 is completely determined by the roughness shape. Appropriate upstream, boundary and  
 14 matching conditions are derived for the problem. Due to the parabolicity, the equations  
 15 are solved efficiently using a marching method to obtain the streaky flow. The instability  
 16 of the streaky flow is shown to be controlled by the spanwise dependent (periodic)  
 17 wall shear. Two- and weakly three-dimensional lower-frequency modes are found to be  
 18 stabilised by the streaks, confirming previous experimental findings, while stronger three-  
 19 dimensional and higher-frequency modes are destabilised. Among the three roughness  
 20 shapes considered, the roughness elements in the form of hemispherical cap is found to  
 21 be most effective for a given height. A resonant subharmonic interaction was found to  
 22 occur for modes with spanwise wavelength twice that of the roughness elements.

23 **Key words:**

---

## 24 1. Introduction

25 Aerodynamic drag has been one of the main focuses of fluid dynamics research. With  
 26 the aim of reducing drag, different flow control technologies have been proposed and  
 27 developed, which can be categorised into active and passive systems. Active systems  
 28 require an energy input to function and are limited mainly to laboratory conditions. Con-  
 29 trolled suction and/or blowing is an example of this type of strategy. Promising results  
 30 with this strategy have been obtained for example by the experimental and numerical  
 31 works of Reynolds & Saric (1986) and Reed & Nayfeh (1986), respectively, who found

<sup>†</sup> Email address for correspondence: ck2415@ic.ac.uk

32 that continuous suction through porous suction strips stabilises Tollmien–Schlichting  
33 (T–S) waves and thereby delays transition to turbulence. For further references of active  
34 boundary-layer flow control and transition control, the reader is referred to Joslin (1998)  
35 and Gad-el Hak (2000).

36 In contrast, passive systems require no energy input and are thus simpler. They are also  
37 more robust and are usually preferred. An example of passive control is the application of  
38 surface roughness elements. It had long been thought that the effect of surface roughness  
39 with respect to drag reduction would be neutral at best. However, the positive effects  
40 of certain forms of surface roughness elements, e.g. riblets, on drag reduction have been  
41 measured (e.g. Walsh 1982, Green 2008). Surface roughness may reduce drag by two  
42 possible ways: affecting fully developed turbulence, and delaying transition.

43 Surface roughness may influence transition through different mechanisms depending on  
44 its location and length scale. When roughness elements are located near the lower branch  
45 neutral positions, and have length scale comparable with that of the instability, they affect  
46 transition through the receptivity process, where instability modes are generated due to  
47 the interaction of the roughness-induced local mean-flow distortion and the free stream  
48 disturbances, such as sound or vorticity (Saric *et al.* 2002). If the roughness is large  
49 enough and located in the main unstable region, it can significantly alter the stability  
50 properties. If the roughness length scale is much longer than the characteristic wavelength  
51 of the instability, a local stability analysis can be applied to the distorted base flow to  
52 account for the effect of the roughness (Klebanoff & Tidstrom 1972, Nayfeh *et al.* 1988).  
53 For the case where the roughness length scale is comparable to the wavelength of the  
54 instability, the distorted base flow cannot be treated as being locally parallel and the  
55 roughness influences transition through a different mechanism, which is referred to as  
56 local scattering (Wu & Hogg 2006). This process was studied theoretically by Wu &  
57 Dong (2016) and numerically by Xu *et al.* (2016). The effect of localised roughness on  
58 transition was characterised naturally by a transmission coefficient, defined as the ratio  
59 of the amplitudes of the T–S wave downstream and upstream of the roughness.

60 A series of experiments have been conducted by Fransson and his collaborators to  
61 investigate the effects of several different surface roughness geometries on the boundary-  
62 layer flow over a flat plate. Their efforts were prompted by instability analysis for  
63 boundary layers perturbed by streaks, which suggested that streaks with an amplitude  
64 below a certain threshold inhibit the amplification of two-dimensional T–S waves (Cossu  
65 & Brandt 2002, 2004). The streaks in these calculations were represented by the so-  
66 called optimal perturbation, which develops from the initial disturbance at an upstream  
67 location with the specific transverse distribution that maximizes the amplitude gain  
68 at a chosen downstream position (Andersson *et al.* 1999; Luchini 2000). Generation  
69 of an optimal disturbance requires a specific distribution across the boundary layer at  
70 a streamwise location. It is probably very difficult to achieve this by viable physical  
71 means. Actuation or forcing is typically deployed at the surface, and they cannot deliver  
72 directly the desired transverse distribution. Use of a ‘body force’ looks more flexible  
73 as it acts on the bulk of the flow field. However, any physical body force, e.g. Lorentz  
74 force and plasma-induced body force, must still be generated by devices (e.g. electro-  
75 magnetic actuation or dielectric barrier discharge) deployed at the surface. To the  
76 best of our knowledge, such optimal disturbances have not yet been generated in the  
77 laboratory. White (2002) demonstrated that streaks induced by a spanwise periodic array  
78 of roughness elements with circular cross section differed from optimal perturbations  
79 in the wall-normal distribution and streamwise evolution, namely, the former are more  
80 confined in the wall region than the latter, and they attain their maximum amplitude and  
81 start to attenuate earlier. These differences, observed for streaks of relative low amplitude,

were shown by Fransson *et al.* (2004) to persist for larger-amplitude streaks generated by a spanwise periodic array of cylindrical roughness elements. Denissen & White (2013) demonstrated further that compared with optimal streaks, roughness-induced streaks are more susceptible to secondary instabilities which lead to transition. Instead of looking for optimal disturbances, several researchers have chosen to investigate streaks generated by external forcing that could be realized in laboratory, or by external disturbances which are present naturally or as a viable control means. Such an external forcing or disturbance must be accounted for explicitly in the mathematical formulation, which is important since the purpose of studying transition is to predict its occurrence in terms of external disturbances and/or control action. It is therefore important to study effects of streaks that can be generated by specific and viable means. Fransson *et al.* (2005) investigated how T-S waves evolved in the presence of such physically generated streaks. They found that generally two-dimensional T-S waves are attenuated and the attenuation increases with streak amplitudes for a range of frequencies. The degree of this damping effect is limited by the streak amplitude because streaks exceeding a certain critical value cause bypass transition. The stabilising role of streaks was further investigated by Fransson *et al.* (2006), who used cylindrical roughness elements to generate streaks, and a two-dimensional suction slot to excite T-S waves of different amplitude. They showed that streaks primarily reduce the exponential growth of small-amplitude T-S waves, but do not cause any destabilization when the T-S wave has acquired a large amplitude. Fransson *et al.* (2006) further demonstrated that stabilization occurs even with the addition of weak white noise to the periodic excitation.

Shahinfar *et al.* (2012) used a new form of roughness elements, referred to as miniature vortex generators (MVGs), to generate streaks. T-S waves were introduced upstream of the roughness elements rather than downstream as in Fransson *et al.* (2006) with the aim to study the effects on the oncoming T-S waves, which is more representative of practical situations. They showed that MVGs were able to generate streaks with larger critical amplitudes when compared with cylindrical elements used previously. The streamwise velocity perturbations reached 32% of the free stream velocity without causing bypass transition. The significant contrast indicates that the structure of streaks and their generator are both relevant. Shahinfar *et al.* (2013) carried out an extensive parametric study of MVGs of various configurations, and in particular an integral-based streak amplitude that accounts for the spanwise structure was introduced to characterise consistently the stabilising effect of roughness of different heights and orientations. Downs & Fransson (2014) showed that streamwise elongated, spanwise periodic roughness elements with hemispherical-cap cross-sections can be effective in delaying transition. These elements have the advantage of being simpler to manufacture and deploy compared with MVGs.

Fransson & Talamelli (2012) and Sattarzadeh *et al.* (2014) investigated the effect of a second row of MVGs placed downstream of the first row. They found that if placed close to the first row, the second row did not contribute much to the cause as the generated streaks typically decayed quickly to levels similar to the case without it. Placing the second row of MVGs further away from the first row generated sustained streaks and greatly increased the performance of this control strategy.

The attenuation of oblique T-S waves in a streaky boundary layer was suggested by nonlinear PSE (parabolised stability equations) calculations (Bagheri & Hanifi 2007), where streaks were taken to develop from optimal perturbations. This possibility was investigated experimentally (Shahinfar *et al.* 2014), where streaks were created by MVGs. In addition to a planar T-S wave, three-dimensional single and a pair of oblique waves were generated upstream of the MVGs. In a small region just behind the MVGs, all

investigated disturbances experienced an overall growth in amplitude. However, the amplitudes of these disturbances were found to be reduced further downstream.

Direct numerical simulation (DNS) of the flow over an array of roughness elements - smooth bumps and MVGs - have been performed by Piot *et al.* (2008) and Siconolfi *et al.* (2015), respectively along with a viscous bi-global stability analysis of the deformed flow. Piot *et al.* (2008) showed that the eigenmodes are the continuation of T–S waves associated with the unperturbed Blasius boundary layer, and their growth rates are reduced for all examined frequencies. Siconolfi *et al.* (2015) found that right behind the MVGs a region of instability exists which was associated with the geometric discontinuity of the MVGs’ shape. However, farther downstream in an extended region where the streaky flow is present, the T–S waves were greatly stabilised.

Using DNS, Xu *et al.* (2017*b*) studied the effect on the oncoming T–S waves of arrays of three-dimensional indentations, and a strong destabilising effect was found, which was attributed to the inflection instability of the separation bubbles caused by the indentation. Xu *et al.* (2017*a*) simulated the impact of smooth forward-facing steps, and interestingly a step was found to stabilise the T–S wave if its height is less than 20% of the local boundary-layer thickness, beyond which it destabilises.

Several theoretical studies of the mean-flow distortion induced by surface roughness elements with different geometries and scalings can be found in the literature. In many studies, a high-Reynolds-number asymptotic approach was taken. Duck & Burggraf (1986) considered roughness with the streamwise and spanwise length scales both being of  $O(R^{-3/8}L)$ , so that the induced flow is governed by the standard triple-deck theory, where  $R = U_\infty L/\nu$  is the Reynolds number, with  $L$  being the distance from the leading edge of the flat plate to the surface roughness,  $U_\infty$  the free-stream velocity and  $\nu$  the kinematic viscosity of the fluid. Rozhko & Ruban (1987) formulated an asymptotic theory for a streamwise elongated roughness on a curved surface, where the characteristic lengths of the roughness in the spanwise and streamwise directions were of  $O(R^{-3/7}L)$  and  $O(R^{-3/14}L)$ , respectively. Note that the characteristic spanwise length is narrower than that for the classical triple-deck formulation. This scaling is distinguished because the pressure variation across the boundary layer, caused by the centrifugal force, comes into play. The solution to the problem was considered by Rozhko *et al.* (1988) in the limits of small roughness height and even longer roughnesses which enhanced the effect of the surface curvature in the pressure-displacement relation. Goldstein *et al.* (2010, 2016) focused on roughness elements that had a spanwise separation of the order of the local boundary-layer thickness whilst the streamwise length was on the triple-deck scale. Their main interest was in the nonlinear wake flow as it gives an appropriate basis to study secondary inviscid instability, which induces bypass transition to turbulence.

The interest of the present study is in spanwise periodic, streamwise elongated roughness elements and their effect on instability. To this end, a high-Reynolds-number approach is adopted. This framework provides a self-consistent method to show the stabilising effect at different frequencies and spanwise wavenumbers. The spanwise scale remains on the triple-deck scale  $O(R^{-3/8}L)$ , since our interest is in the impact on the lower-branch T–S waves, whose spanwise wavelength is on this scale. The streamwise length of the roughness is much longer than the triple-deck scale, in accordance with experiments. In order to calculate the flow induced by such a form of roughness elements, our strategy is to take the formulation of Duck & Burggraf (1986), and introduce a new set of “stretched” or “compressed” variables depending on the aspect ratio of the roughness. Then, the balances of dominant terms in the momentum and continuity equations would reveal a new set of boundary-layer equations, which are much easier to solve than the full triple-deck system or N–S equations. The solutions are then interpreted and

182 finally compared with the experimental results mainly of Downs & Fransson (2014). A  
 183 linear stability analysis was conducted on the streaky base flow produced by the surface  
 184 roughness in order to further explore their effect on transition.

185 The present high-Reynolds-number asymptotic approach is to complement the finite-  
 186 Reynolds-number calculations of Piot *et al.* (2008) and Siconolfi *et al.* (2015). First, it  
 187 provides a simple and effective tool to assess the impact of the roughness on the boundary-  
 188 layer flow and on its stability. Second, it reduces the computationally expensive viscous  
 189 bi-global eigenvalue problem to a one-dimensional one in the spanwise direction and  
 190 moreover the wall shear is shown to be the quantity directly controlling the instability  
 191 of the streaky boundary layer, a result shedding light on the essential mechanism of the  
 192 stabilisation. Third, the asymptotic framework allows us to establish that the stabilising  
 193 effect, observed in experiments and confirmed by bi-global analysis (Piot *et al.* 2008;  
 194 Siconolfi *et al.* 2015), is not restricted to a finite range of Reynolds numbers, but  
 195 operates at all Reynolds numbers sufficiently high.

196 The rest of the paper is organised as follows. In §2, the problem is formulated starting  
 197 from the triple-deck theory, and based on the aspect ratio of the roughness element, the  
 198 set of fully nonlinear governing equations is derived, and the numerical procedures to solve  
 199 the equations governing nonlinear streaks are introduced. The numerical results about  
 200 streaks are presented in §3. The linear stability analysis of the streaky flow is performed  
 201 in §4, where we show that the instability is controlled by the spanwise dependent wall  
 202 shear  $\lambda_u(Z)$ . The numerical procedure for solving the linear stability is described. In §5,  
 203 we present the numerical results on the instability. A summary and further discussions  
 204 are given in §6.

## 205 2. Problem formulation

We consider the boundary-layer flow on a flat plate, on which an array of spanwise  
 periodic and streamwise isolated (but elongated) roughness elements are present at a  
 distance  $L$  from the leading edge. The flow is described using the Cartesian coordinate  
 system  $(x, y, z)$  with its origin located at the centre of the hump, where  $x$  and  $y$  are  
 along and normal to the wall respectively while  $z$  indicates the spanwise direction. The  
 velocities in the  $(x, y, z)$  directions are denoted by  $(u, v, w)$ . The coordinates are non-  
 dimensionalised by  $L$ , the velocities by  $U_\infty$ , time  $t$  by  $L/U_\infty$ , and pressure  $p$  by  $\rho U_\infty^2$ ,  
 where  $U_\infty$  is the speed of the oncoming flow and  $\rho$  the density of the fluid. We start  
 with the generic case, where the streamwise and spanwise length scales of the roughness  
 elements are both of  $O(R^{-3/8}L)$ , and their height is of  $O(R^{-5/8}L)$ , where  $R$  is the  
 Reynolds number based on  $L$ . The mean flow is described by the triple-deck structure,  
 as was shown by Smith *et al.* (1977). The theory is facilitated by introducing the rescaled  
 coordinates,

$$X = x/\epsilon^3 = O(1), \quad Z = z/\epsilon^3 = O(1), \quad Y = y/\epsilon^5 = O(1). \quad (2.1a - c)$$

206 The small parameter,  $\epsilon = R^{-1/8}$  and the roughness elements are centred at  $X = 0$ . In  
 207 terms of  $Y$ , the geometry of the roughness is specified as

$$Y = hF(X, Z), \quad (2.2)$$

208 where  $h$  is the rescaled height, and  $F$  characterises the shape.

209 In the main deck, the transverse variable  $\tilde{y} = y/\epsilon^4 = O(1)$ , and the velocity components

and pressure are expressed as (Smith *et al.* 1977; Duck & Burggraf 1986):

$$u = U_B(\tilde{y}) + \epsilon A(X, Z)U_B'(\tilde{y}) + O(\epsilon^2), \quad (2.3a)$$

$$v = -\epsilon^2 \frac{\partial A}{\partial X} U_B(\tilde{y}) + O(\epsilon^3), \quad (2.3b)$$

$$w = \frac{\epsilon^2 D(X, Z)}{U_B(\tilde{y})} + O(\epsilon^3), \quad \text{where} \quad \frac{\partial D}{\partial X} = -\frac{\partial P}{\partial Z}, \quad (2.3c)$$

$$p = \epsilon^2 P(X, Z) + O(\epsilon^3), \quad (2.3d)$$

where  $U_B(\tilde{y}) = F'(\tilde{y})$  is the Blasius velocity profile determined by  $F''' + \frac{1}{2}FF'' = 0$  subject to the boundary conditions:  $F(0) = F'(0) = 0$  and  $F' \rightarrow 1$  as  $\tilde{y} \rightarrow \infty$ , and  $A(X, Z)$  is the displacement function; here a prime denotes differentiation with respect to  $\tilde{y}$ . The displacement function,  $A$ , describes how the viscous motion in the boundary layer and surface roughness (if exists) impacts the inviscid part of the flow field. It can be interpreted as displacing the streamlines at the outer edge of the boundary layer by an amount proportional to  $A$ . In the standard triple-deck theory, due to its relatively rapid streamwise variation the displacement effect induces a pressure gradient that is large enough to act on the viscous motion simultaneously (Stewartson & Williams 1969; Neiland 1969; Messiter 1970). As a result,  $A$  has to be obtained along with the velocity field as part of the solution.

Because the transverse velocity,  $v$ , does not vanish as  $\tilde{y} \rightarrow \infty$ , an upper deck must be introduced, where  $y^\dagger = \epsilon^{-3}y = O(1)$ . The transverse velocity induces a pressure, which may be written as  $p = \epsilon^2 P^\dagger$ . The scaled pressure  $P^\dagger$  satisfies the Laplace equation,

$$\left[ \frac{\partial^2}{\partial X^2} + \frac{\partial^2}{\partial y^{\dagger 2}} + \frac{\partial^2}{\partial Z^2} \right] P^\dagger = 0 \quad \text{with} \quad \frac{\partial P^\dagger}{\partial y^\dagger} \Big|_{y^\dagger=0} = \frac{\partial^2 A}{\partial X^2} \quad \text{and} \quad P^\dagger \rightarrow 0 \quad \text{as} \quad y^\dagger \rightarrow \infty, \quad (2.4)$$

where the boundary condition follows from asymptotically matching the main- and upper-deck solutions. Solving the boundary-value problem (2.4), one obtains the pressure-displacement relation (Smith *et al.* 1977; Duck & Burggraf 1986),

$$P(X, Z) \equiv P^\dagger(X, Z, 0) = -\frac{1}{2\pi} \int_{-\infty}^{\infty} \int_{-\infty}^{\infty} \frac{\partial^2 A / \partial \vartheta^2}{[(X - \vartheta)^2 + (Z - \zeta)^2]^{1/2}} d\vartheta d\zeta. \quad (2.5)$$

The main-deck solution (2.3a) fails to satisfy the no-slip boundary condition at the wall, and hence a viscous lower deck is introduced, which has an  $O(R^{-5/8}L)$  thickness. The velocity and pressure scale as,

$$(u, v, w, p) = (\epsilon U, \epsilon^3 V, \epsilon W, \epsilon^2 P). \quad (2.6)$$

In terms of  $(X, Y, Z)$  and  $(U, V, W, P)$ , the equations governing the flow in the lower deck read,

$$\frac{\partial U}{\partial X} + \frac{\partial V}{\partial Y} + \frac{\partial W}{\partial Z} = 0, \quad (2.7a)$$

$$U \frac{\partial U}{\partial X} + V \frac{\partial U}{\partial Y} + W \frac{\partial U}{\partial Z} = -\frac{\partial P}{\partial X} + \frac{\partial^2 U}{\partial Y^2}, \quad (2.7b)$$

$$U \frac{\partial W}{\partial X} + V \frac{\partial W}{\partial Y} + W \frac{\partial W}{\partial Z} = -\frac{\partial P}{\partial Z} + \frac{\partial^2 W}{\partial Y^2}, \quad (2.7c)$$

where, similarly to other boundary-layer-type equations, the streamwise and spanwise diffusion are negligible, because the respective spatial scales are a factor of  $O(\epsilon^{-2})$  longer

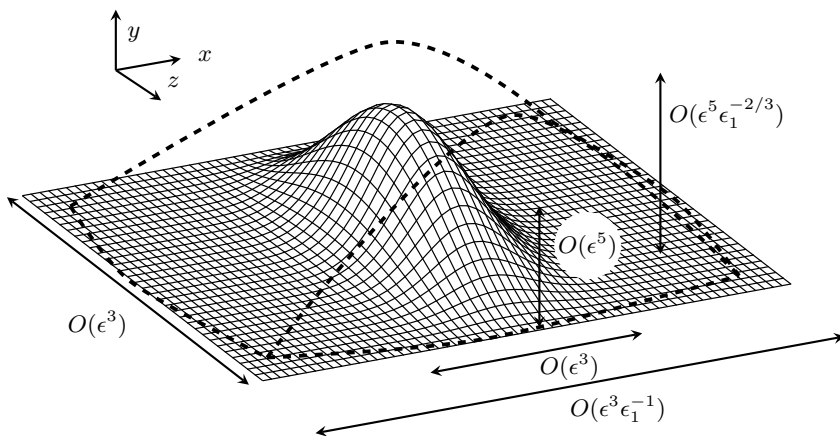


FIGURE 1. A sketch showing the dimensions of an elongated roughness element relative to the triple-deck scale. The solid lines indicate the dimensions and height of an element on the triple-deck scale, while the dashed lines represent those of an elongated element.

237 than the wall-normal scale. These equations are subject to the boundary and matching  
238 conditions,

$$U = V = W = 0 \quad \text{on} \quad Y = hF(X, Z), \quad (2.8a)$$

$$U \sim \lambda_B[Y + A(X, Z)], \quad W \sim \frac{D(X, Z)}{\lambda_B Y} \quad \text{as} \quad Y \rightarrow \infty, \quad (2.8b)$$

$$U \sim \lambda_B Y, \quad V, W, P \rightarrow 0 \quad \text{as} \quad X \rightarrow -\infty \quad \text{with} \quad \frac{\partial D}{\partial X} = -\frac{\partial P}{\partial Z}, \quad (2.8c)$$

239 where  $\lambda_B = U'_B(0) = 0.33206$  is the wall shear of the unperturbed base flow. As in Duck  
240 & Burggraf (1986), it is convenient to introduce the Prandtl transposition (Prandtl 1938),

$$\tilde{Y} = Y - hF(X, Z), \quad \tilde{V} = V - Uh \frac{\partial F}{\partial X} - Wh \frac{\partial F}{\partial Z}. \quad (2.9)$$

241 Equations (2.7a-c) as well as boundary and matching conditions, (2.8a,c), remain  
242 unchanged with  $\tilde{Y}$  and  $\tilde{V}$  replacing  $Y$  and  $V$  respectively, while the matching conditions  
243 (2.8b) become

$$U \sim \lambda_B(\tilde{Y} + A(X, Z) + hF(X, Z)), \quad W \sim \frac{D(X, Z)}{\lambda_B \tilde{Y}} \quad \text{as} \quad \tilde{Y} \rightarrow \infty. \quad (2.10)$$

244 The standard triple-deck equations are elliptic in both the streamwise and spanwise  
245 directions. Roughness on the standard triple-deck scale acts as a scatter to influence the  
246 development of oncoming T-S waves. The local scattering theory of Wu & Dong (2016)  
247 can be easily extended to the present three-dimensional case, but this would lead to  
248 a mathematical system that is quite challenging to solve numerically. In the following  
249 we will consider arrays of roughness elements which are elongated in the streamwise  
250 direction. The effect of the distorted mean flow can be accounted for by a linear stability  
251 analysis that is local in the streamwise direction, but global in the spanwise direction.  
252 This is a much simpler problem than the full three-dimensional local scattering.

## 2.1. Nonlinear formulation for elongated roughness

253  
254  
255  
256  
257  
258  
259  
260  
261  
262

We now consider elongated roughness elements, whose spanwise length scale  $\Lambda^*$  remains  $O(R^{-3/8}L)$ , but the streamwise length scale  $L_x^*$  is much longer by a factor  $O(\epsilon_1^{-1})$ , where  $\epsilon_1 = \Lambda^*/L_x^* \ll 1$  will be referred to as the aspect ratio. The appropriate asymptotic description of the induced mean flow can of course be derived from the N–S equations, but the better option is to deduce the governing equations and the boundary/matching conditions from the standard triple-deck system through rescaling and then taking the limit  $\epsilon_1 \rightarrow 0$ . The spanwise scaling is left unchanged, but the streamwise coordinate is stretched. The coordinates, as well as the velocity, pressure and displacement function must be rescaled as

$$\left. \begin{aligned} (\hat{X}, \hat{Y}, \hat{Z}) &= (\lambda_B^{5/4} \epsilon_1 X, \lambda_B^{3/4} \epsilon_1^{1/3} \tilde{Y}, \lambda_B^{5/4} Z), \\ (\hat{U}, \hat{V}, \hat{W}) &= (\lambda_B^{-1/4} \epsilon_1^{1/3} U, \lambda_B^{-3/4} \epsilon_1^{-1/3} \tilde{V}, \lambda_B^{-1/4} \epsilon_1^{-2/3} W), \\ (\hat{P}, \hat{A}) &= (\lambda_B^{-1/2} \epsilon_1^{-4/3} P, \lambda_B^{3/4} \epsilon_1^{2/3} A), \end{aligned} \right\} \quad (2.11)$$

263  
264  
265  
266  
267  
268  
269  
270  
271  
272

where the rescaling with respect to  $\lambda_B$  is the standard one (Smith *et al.* 1977), and of importance is the rescaling or ‘stretching’ involving  $\epsilon_1$ . The respective scales were found by the appropriate balances as follows. In the continuity equation (2.7a), all three terms balance. In the  $x$ -momentum equation (2.7b) the inertial and viscous terms balance, while in the  $z$ -momentum equation (2.7c), the inertial, pressure gradient and viscous terms balance. In addition, the terms in the matching condition (2.10) and the pressure displacement relation (2.5) balance respectively. The seven relations obtained this way determine the velocity and pressure scaling factors in terms of  $\epsilon_1$ . The details of the derivation is given in Kátaı (2020). In order for the roughness-induced mean-flow distortion to be nonlinear, the height must be sufficiently large, and be scaled as,

$$\hat{h} = \epsilon_1^{2/3} \lambda_B^{3/4} h = O(1). \quad (2.12)$$

273  
274

A sketch of the coordinate stretching can be seen in figure 1. The asymptotic expansion for the displacement function is

$$\hat{A} = -\hat{h}F(\hat{X}, \hat{Z}) + \epsilon_1^{1/3} \hat{A}_1 + \dots \quad (2.13)$$

275

Subject to the Prandtl transposition (2.9), the governing equations are:

$$\frac{\partial \hat{U}}{\partial \hat{X}} + \frac{\partial \hat{V}}{\partial \hat{Y}} + \frac{\partial \hat{W}}{\partial \hat{Z}} = 0, \quad (2.14a)$$

276

$$\hat{U} \frac{\partial \hat{U}}{\partial \hat{X}} + \hat{V} \frac{\partial \hat{U}}{\partial \hat{Y}} + \hat{W} \frac{\partial \hat{U}}{\partial \hat{Z}} = \frac{\partial^2 \hat{U}}{\partial \hat{Y}^2}, \quad (2.14b)$$

277

$$\hat{U} \frac{\partial \hat{W}}{\partial \hat{X}} + \hat{V} \frac{\partial \hat{W}}{\partial \hat{Y}} + \hat{W} \frac{\partial \hat{W}}{\partial \hat{Z}} = -\frac{\partial \hat{P}}{\partial \hat{Z}} + \frac{\partial^2 \hat{W}}{\partial \hat{Y}^2}, \quad (2.14c)$$

278

and after the rescaling the boundary and matching conditions, (2.8a,c) and (2.10), read

$$\hat{U} = \hat{V} = \hat{W} = 0 \quad \text{on} \quad \hat{Y} = 0, \quad (2.15a)$$

$$\hat{U} \sim \hat{Y} + \hat{A}_1(\hat{X}, \hat{Z}), \quad \hat{W} \sim \frac{\hat{D}(\hat{X}, \hat{Z})}{\hat{Y}} \quad \text{as} \quad \hat{Y} \rightarrow \infty, \quad (2.15b)$$

$$\hat{U} \sim \hat{Y}, \quad \hat{V}, \hat{W}, \hat{P} \rightarrow 0 \quad \text{as} \quad \hat{X} \rightarrow -\infty \quad \text{with} \quad \frac{\partial \hat{D}}{\partial \hat{X}} = -\frac{\partial \hat{P}}{\partial \hat{Z}}. \quad (2.15c)$$

279

With the streamwise length much longer than the triple-deck scale, the streamwise



280 derivative in the Laplace equation (2.4) becomes negligible due to the rescaling (2.11).  
 281 This reduced quasi-two-dimensional Laplace equation, subject to the Neumann boundary  
 282 condition in (2.4), is solved to give the leading-order pressure,

$$\hat{P}(\hat{X}, \hat{Z}) = \frac{\hat{h}}{\pi} \int_{-\infty}^{\infty} \frac{\partial^2 F(\hat{X}, \zeta)}{\partial \hat{X}^2} \ln |\hat{Z} - \zeta| d\zeta, \quad (2.16)$$

283 where use has been made of (2.13). The above pressure-displacement relation is found to  
 284 be consistent with equation (1.3) of Rozhko *et al.* (1988) with  $\chi_0 = 0$  (due to the absence  
 285 of centrifugal force). Note that with the scaling (2.12), the three velocity components are  
 286 fully coupled and the flow is fully three-dimensional. Nevertheless the system (2.14) with  
 287 (2.16) is parabolic in  $\hat{X}$ , since the pressure (to leading order) is completely determined by  
 288 the roughness geometry. A similar result for ‘long’ two-dimensional humps was obtained  
 289 by Smith *et al.* (1981), where the pressure to leading order was completely determined  
 290 by the roughness shape. However, the streamwise pressure gradient appears in their  
 291 boundary-layer equations, whereas in the present formulation the spanwise pressure  
 292 gradient appears in the three-dimensional governing equations (2.14). Intuitively, the  
 293 reason for the streamwise pressure gradient to be negligible is that it becomes weaker as  
 294 the streamwise length becomes longer. Formally, it is a factor of  $O(\epsilon_1^2)$  smaller than the  
 295 inertial and viscous terms in the streamwise momentum equation as can be shown by  
 296 applying the rescaling (2.11) to (2.7b).

297 Due to its parabolic nature, the asymptotically reduced system (2.14)–(2.16) can be  
 298 solved by efficient marching methods without the need of specifying a downstream  
 299 condition or introducing an artificial buffer region. The application of the Prandtl  
 300 transformation makes meshing unnecessary. These lead to a significant reduction in  
 301 computational complexity and costs in comparison with solving the steady N–S equations,  
 302 which requires careful meshing as well as sufficiently fine spatial and temporal resolutions  
 303 for high-Reynolds-number flows of interest.

304 The present theory remains valid as long as the wall layer of the streaky flow is  
 305 submerged within the main boundary layer over the curved surface, that is,  $\epsilon^5 \epsilon_1^{-1/3} \ll \epsilon^4$ ,  
 306 which gives  $\epsilon_1 \gg \epsilon^3$ . In the limiting case, the roughness height can be as large as  $O(\epsilon^3 L)$ ,  
 307 much greater than the  $O(\epsilon^4 L)$  local boundary-layer thickness, while its streamwise length  
 308 scale becomes comparable with  $L$ . Such roughness element arrays thus appear like  
 309 longitudinal riblets and grooves, which are of considerable interest as well and are being  
 310 investigated by the authors.

311 The validity of the present theory covers roughness elements with heights comparable  
 312 to the local boundary-layer thickness, for which  $\epsilon_1 = O(\epsilon^{3/2})$ . For general aviation and  
 313 large commercial aircrafts, the flight speeds are about 900 km/h and the chord lengths  
 314 are in the range of 4–8 m, with the Reynolds numbers being  $10^7 - 10^8$ . A representative  
 315 situation would be roughness elements centred at  $L = 0.1$  m from the leading edge,  
 316 where the Reynolds number  $R \approx 2 \times 10^6$ , giving  $\epsilon = 0.16$  and the displacement thickness  
 317  $\delta^* \approx 0.12$  mm (the corresponding nominal thickness where the speed is 99% of the  
 318 free-stream velocity is  $\delta_{0.99}^* \approx 0.60$  mm). The roughness spanwise dimension or spacing  
 319 is comparable to the characteristic wavelength  $\lambda_{TS} \epsilon^3 \lambda_B^{-5/4} L \approx 5.2$  mm, where  $\lambda_{TS} =$   
 320  $2\pi/\alpha$  with  $\alpha = 2$  taken to be the wavenumber of the most unstable T–S mode. As a  
 321 rule of thumb, we take  $\epsilon_1 = 0.1$  for the present theory to be applicable, and so the  
 322 corresponding roughness elements would have a streamwise length of about 52 mm,  
 323 while the height would be  $\lambda_B^{-3/4} \epsilon^5 \epsilon_1^{-2/3} L \approx 0.12$  mm. Deployment of roughness elements  
 324 with dimensions in the above range could lead to an effective stabilizing effect. Such  
 325 roughness elements could also be present on wings due to manufactory imperfections and

326 installation reasons. Screws (bolts and nuts) and gaps (indentations), which are common  
 327 forms of roughness, are not elongated, and their effects may be quantified by a three-  
 328 dimensional extension of the local scattering theory (Wu & Dong 2016) if their streamwise  
 329 and spanwise dimensions are  $\lambda_{TS}\lambda_B^{-5/4}\epsilon^3L \approx 5$  mm, and height  $\lambda_B^{-3/4}\epsilon^5L \approx 0.06$  mm.  
 330 In either cases, the roughness elements capable of influencing transition are fairly small,  
 331 about 10 times as large as the average 10-micron surface finish of a modern aircraft. Of  
 332 course, the curvature and/or swept configuration of a real wing would complicate and  
 333 even change the role of roughness.

## 334 2.2. Boundary and initial conditions for the fully nonlinear formulation

335 In order to obtain appropriate numerical solutions to the nonlinear formulation (2.14)–  
 336 (2.16), suitable upstream and far-field asymptotic boundary conditions need to be found.

### 337 2.2.1. Upstream conditions

338 In the upstream limit  $\hat{X} \rightarrow -\infty$ ,  $F(\hat{X}, \hat{Z}) \rightarrow 0$  and so the deviation from the Blasius  
 339 flow is small. Hence, the nonlinear terms in the governing equations (2.14) can be  
 340 neglected. By writing

$$\hat{U} = \hat{Y} + \hat{U}_d, \quad (2.17)$$

with  $\hat{U}_d \ll 1$ , the nonlinear equations (2.14) become the following linear equations,

$$\frac{\partial \hat{U}_d}{\partial \hat{X}} + \frac{\partial \hat{V}}{\partial \hat{Y}} + \frac{\partial \hat{W}}{\partial \hat{Z}} = 0, \quad \hat{Y} \frac{\partial \hat{U}_d}{\partial \hat{X}} + \hat{V} = \frac{\partial^2 \hat{U}_d}{\partial \hat{Y}^2}, \quad \hat{Y} \frac{\partial \hat{W}}{\partial \hat{X}} = -\frac{\partial \hat{P}}{\partial \hat{Z}} + \frac{\partial^2 \hat{W}}{\partial \hat{Y}^2}, \quad (2.18a - c)$$

341 with the boundary and matching conditions (2.15) becoming the following,

$$\hat{U}_d = \hat{V} = \hat{W} = 0 \quad \text{on} \quad \hat{Y} = 0, \quad (2.19a)$$

$$\hat{U}_d \sim \hat{A}_1(\hat{X}, \hat{Z}) \quad \text{and} \quad \hat{W} \sim \frac{\hat{D}(\hat{X}, \hat{Z})}{\hat{Y}} \quad \text{as} \quad \hat{Y} \rightarrow \infty, \quad (2.19b)$$

$$\hat{U}_d, \hat{V}, \hat{W}, \hat{P} \rightarrow 0 \quad \text{as} \quad \hat{X} \rightarrow -\infty \quad \text{with} \quad \partial \hat{D} / \partial \hat{X} = -\partial \hat{P} / \partial \hat{Z}. \quad (2.19c)$$

342 Note that the pressure  $\hat{P}$  is pre-determined by using (2.16), but  $\hat{A}_1$  is part of the solution  
 343 and has to be obtained along with the velocity field.

344 To fix the idea, we assume that the wall shape is of the variable separation form,

$$F(\hat{X}, \hat{Z}) = f(\hat{X})g(\hat{Z}), \quad (2.20)$$

where  $f$  and  $g$  characterise the roughness shape in the streamwise and spanwise directions  
 respectively. The velocities far upstream (as  $\hat{X} \rightarrow -\infty$ ) serve as the initial conditions  
 for the numerical marching method. In this region, we seek a similarity solution to the  
 velocities, which, along with the pressure to leading order, can be written as

$$\hat{W} = \hat{h}S'(\hat{Z})T(\hat{X})M(\chi), \quad \hat{U}_d = \hat{h}S''(\hat{Z})Q(\hat{X})G(\chi), \quad \hat{P} = \hat{h}f''(\hat{X})S(\hat{Z}), \quad (2.21a - c)$$

345 where the form of  $\hat{P}$  follows from inserting (2.20) into (2.16), while those of  $\hat{W}$  and  $\hat{U}_d$   
 346 are deduced using (2.18c) and (2.18a), respectively, and  $S$  is given by

$$S(\hat{Z}) = \frac{1}{\pi} \int_{-\infty}^{\infty} g(\zeta) \ln |\hat{Z} - \zeta| d\zeta, \quad (2.22)$$

347  $\chi$  is the similarity variable, and  $T(\hat{X})$  and  $Q(\hat{X})$  are the functions that are to be found  
 348 according to the specific roughness shape to be considered.

349 For a surface shape

$$f(\hat{X}) = \exp(-(\hat{X}/d)^2), \quad (2.23)$$

we insert expressions (2.21) into (2.18c) subject to the boundary conditions in (2.19). The similarity variable,  $\chi$ , and  $T(\hat{X})$  are found to be

$$\chi = 2^{1/3}d^{-2/3}(-\hat{X})^{1/3}\hat{Y}, \quad T(\hat{X}) = -2^{4/3}d^{-8/3}(-\hat{X})^{4/3}\exp(-(\hat{X}/d)^2). \quad (2.24a, b)$$

350 Solving for  $M(\chi)$ , we obtain

$$M(\chi) = -\pi \left[ 3^{-1/2}\text{Ai}(\chi) - \text{Gi}(\chi) \right], \quad (2.25)$$

351 where  $\text{Ai}(\chi)$  and  $\text{Gi}(\chi)$  are the Airy and Scorer's functions, respectively (Abramowitz &  
352 Stegun 1964). On the other hand, substituting (2.21) into (2.18b), differentiating it with  
353 respect to  $\hat{Y}$  and using (2.18a) as well as (2.19), we obtain

$$Q(\hat{X}) = -2^{1/3}d^{-2/3}3^{-2/3}\Gamma(1/3)(-\hat{X})^{1/3}\exp(-(\hat{X}/d)^2), \quad (2.26)$$

354

$$G(\chi) = \frac{3^{2/3}}{\Gamma(1/3)} \left[ \Gamma(1/3) 3^{1/3} \int_0^\chi \text{Ai}(t)dt + \pi 3^{-1/2}\text{Ai}(\chi) - \pi\text{Gi}(\chi) \right], \quad (2.27)$$

355 where  $\Gamma(\cdot)$  is the Gamma function. Then, from the continuity equation (2.18a) and the  
356 no-slip condition at the wall, follows the leading-order vertical velocity component. In  
357 summary, the velocities in the boundary layer far upstream ( $\hat{X} \rightarrow -\infty$ ) are found as,

$$\hat{U} = \hat{Y} + \hat{h}S''(\hat{Z})Q(\hat{X})G(\chi) + \dots, \quad (2.28a)$$

$$\hat{W} = \hat{h}S'(\hat{Z})T(\hat{X})M(\chi) + \dots, \quad (2.28b)$$

$$\hat{V} = -\hat{h}S''(\hat{Z}) \int_0^{\hat{Y}} \left[ T(\hat{X})M(\chi) + Q'(\hat{X})G(\chi) + Q(\hat{X})\chi_{\hat{X}}G'(\chi) \right] d\hat{Y} + \dots. \quad (2.28c)$$

### 358 2.2.2. Behaviour at the outer edge of the lower deck

359 For  $\hat{Y} \gg 1$ , the first few terms of the expansions for the lower-deck velocities are found  
360 to be,

$$\hat{U} = \hat{Y} + \hat{A}_1 + \frac{\hat{h}S''(\hat{Z})f(\hat{X})}{\hat{Y}} \left( 1 - \frac{\hat{A}_1(\hat{X}, \hat{Z})}{\hat{Y}} \right) + \dots, \quad (2.29a)$$

361

$$\hat{V} = -\frac{\partial \hat{A}_1}{\partial \hat{X}} (\hat{Y} + \hat{A}_1) - \hat{h}S''(\hat{Z})f'(\hat{X}) + \frac{\hat{h}}{\hat{Y}} \left( f'S' \frac{\partial \hat{A}_1}{\partial \hat{Z}} - S''f \frac{\partial \hat{A}_1}{\partial \hat{X}} \right) + \dots, \quad (2.29b)$$

$$\hat{W} = -\frac{\hat{h}S'(\hat{Z})}{\hat{Y}} \left\{ f'(\hat{X}) - \frac{f'(\hat{X})\hat{A}_1}{\hat{Y}} + \frac{1}{\hat{Y}^2} \left( f'\hat{A}_1^2 - \hat{h}S'' \int_{-\infty}^{\hat{X}} f(\vartheta)f''(\vartheta)d\vartheta \right) d\vartheta \right\} + \dots. \quad (2.29c)$$

### 362 2.2.3. Step-like wall geometry

363 Another roughness element geometry of relevance is  $F(\hat{X}, \hat{Z}) = f(\hat{X})g(\hat{Z})$ , but with

$$f(\hat{X}) = \frac{1}{2} \left[ \tanh \left( \frac{\hat{X} + l_x}{d_x} \right) - \tanh \left( \frac{\hat{X} - l_x}{d_x} \right) \right], \quad (2.30)$$

364

$$\bar{g}(\hat{Z}) = \begin{cases} \left( \sqrt{d_z^2 - \hat{Z}^2} - d_z + h_z \right) / h_z & \text{for } -l_z < \hat{Z} < l_z, \\ 0, & \text{otherwise,} \end{cases} \quad (2.31)$$

365 where  $\bar{g}(\hat{Z})$  represents the spanwise shape within one period, and  $l_z = \sqrt{d_z^2 - (d_z - h_z)^2}$ .  
366 This shape was chosen because it represents more closely the roughness in the experiment  
367 of Downs & Fransson (2014), which has step-like geometry and hemispherical cap shape

368 in the streamwise and spanwise directions, respectively, but is still relatively smooth as  
 369 required by numerical calculations. Here  $d_z$  is the radius of the sphere and  $h_z$  the height  
 370 of the cap. The parameter  $d_x$  is a measure of steepness of the slopes and  $l_x$  represents the  
 371 length of the roughness element in the streamwise direction. Noting that as  $\hat{X} \rightarrow -\infty$ ,

$$f(\hat{X}) \rightarrow \exp(2\hat{X}/d_x) [\exp(2l_x/d_x) - \exp(-2l_x/d_x)] + O(\exp(4\hat{X})), \quad (2.32)$$

372 a similar procedure to that employed for the Gaussian streamwise shape (2.23) can be  
 373 applied, but this time we have

$$T(\hat{X}) = -2^{4/3} d_x^{-4/3} [\exp(2l_x/d_x) - \exp(-2l_x/d_x)] \exp(2\hat{X}/d_x), \quad (2.33a)$$

374

$$Q(\hat{X}) = -2^{1/3} d_x^{-1/3} \mathfrak{z}^{-2/3} \Gamma(1/3) [\exp(2l_x/d_x) - \exp(-2l_x/d_x)] \exp(2\hat{X}/d_x), \quad (2.33b)$$

375 while the expressions for  $M(\chi)$  and  $G(\chi)$  are the same as (2.25) and (2.27), respectively,  
 376 but with  $\chi = 2^{1/3} d_x^{-1/3} \hat{Y}$ . The streamwise and spanwise velocities in the upstream far  
 377 field are of the same form as (2.28a, b) but the transverse velocity is given by

$$\hat{V} = -\hat{h} S''(\hat{Z}) \left[ T(\hat{X}) \int_0^{\hat{Y}} M(\chi) d\hat{Y} + Q'(\hat{X}) \int_0^{\hat{Y}} G(\chi) d\hat{Y} \right] + \dots \quad (2.34)$$

378

379

### 2.3. Composite solution

380 The solutions for the lower- and main-deck velocities are valid only in their respective  
 381 layers, but a composite solution, uniformly valid across the whole boundary layer, can  
 382 be constructed from them. On noting the rescalings (2.3), (2.6) and (2.11) the usual  
 383 composite solution is formed as (Van Dyke 1975)

$$u^c = \underbrace{\lambda_B^{1/4} R_x^{-1/8} \epsilon_1^{-1/3} \hat{U}(\hat{X}, \hat{Y}, \hat{Z})}_{\text{lower deck expansion}} + \underbrace{U_B(\eta) + \lambda_B^{3/4} R_x^{-1/8} \epsilon_1^{-1/3} \hat{A}_1(\hat{X}, \hat{Z}) U_B'(\eta)}_{\text{main deck expansion}} \\ - \underbrace{\lambda_B^{1/4} R_x^{-1/8} \epsilon_1^{-1/3} (\hat{Y} + \hat{A}_1(\hat{X}, \hat{Z}))}_{\text{common part}}, \quad (2.35)$$

384 where the Reynolds number,  $R_x$ , and the similarity variable,  $\eta$ , are related to the  
 385 dimensional distance from the leading edge,  $x^* = L(x+1)$ , as follows,

$$R_x = U_\infty x^* / \nu \quad \text{and} \quad \eta = y^* \sqrt{U_\infty / \nu x^*} = \tilde{y} \sqrt{L/x^*}, \quad (2.36)$$

386 where  $y^*$  is the wall-normal dimensional distance. We will decompose the lower-deck  
 387 solution as  $\hat{U} = \hat{Y} + \hat{U}_d$  with  $\hat{U}_d = O(1)$  representing the roughness induced streaks in  
 388 the vicinity of the roughness. The composite solution is

$$u^c = U_B(\eta) + \lambda_B^{1/4} R_x^{-1/8} \epsilon_1^{-1/3} [\hat{U}_d(\hat{X}, \hat{Y}, \hat{Z}) + \hat{A}_1(\hat{X}, \hat{Z}) (U_B'(\eta) / \lambda_B - 1)]. \quad (2.37)$$

389

### 2.4. Numerical procedures for the streaky base flow

390 To facilitate the numerical calculations, we introduce the dependent variables,

$$\hat{U}_d = \hat{U} - \hat{Y} \quad \text{and} \quad \tau_d = \frac{\partial \hat{U}_d}{\partial \hat{Y}}. \quad (2.38)$$

391 Clearly  $\hat{U}_d$  represents the distortion caused by the roughness. The velocities were repre-  
 392 sented as Fourier series to take advantage of the periodic nature of the problem,

$$(\tau_d, \hat{W}, \hat{V}, \hat{U}_d) = \sum_{n=-\infty}^{\infty} (\tau_{dn}, \hat{W}_n, \hat{V}_n, \hat{U}_{dn}) e^{in\beta\hat{Z}}, \quad (2.39)$$

393 where  $\beta = 2\pi/\Lambda$ . After differentiating (2.14b) and rearranging the equations using the  
 394 new variables in Fourier space, equations (2.14) become,

$$\hat{Y} \frac{\partial \hat{W}_n}{\partial \hat{X}} - \frac{\partial^2 \hat{W}_n}{\partial \hat{Y}^2} = -in\beta(\mathcal{F}(\hat{P}))_n + (\mathcal{F}(N_3))_n, \quad (2.40a)$$

395

$$\hat{Y} \frac{\partial \tau_{dn}}{\partial \hat{X}} - \frac{\partial^2 \tau_{dn}}{\partial \hat{Y}^2} = in\beta \hat{W}_n + (\mathcal{F}(N_1))_n, \quad (2.40b)$$

396

$$\hat{V}_n = - \int_0^{\hat{Y}} \left( in\beta \hat{W}_n + \frac{\partial \hat{U}_{dn}}{\partial \hat{X}} \right) d\hat{Y}, \quad (2.40c)$$

397 where  $\mathcal{F}(\cdot)$  denotes a discrete-Fourier-transformed quantity, similar to the expressions in  
 398 (2.39), and the non-linear terms,  $N_3$  and  $N_1$ , are as follows,

$$N_1 = -\hat{W} \frac{\partial \tau_d}{\partial \hat{Z}} + \tau_d \frac{\partial \hat{W}}{\partial \hat{Z}} - \hat{U}_d \frac{\partial \tau_d}{\partial \hat{X}} - \hat{V} \frac{\partial \tau_d}{\partial \hat{Y}} - \frac{\partial \hat{W}}{\partial \hat{Y}} \frac{\partial \hat{U}_d}{\partial \hat{Z}}, \quad (2.41a)$$

$$N_3 = -\hat{U}_d \frac{\partial \hat{W}}{\partial \hat{X}} - \hat{V} \frac{\partial \hat{W}}{\partial \hat{Y}} - \hat{W} \frac{\partial \hat{W}}{\partial \hat{Z}}. \quad (2.41b)$$

399 Equation (2.40b) is subject to the Neumann boundary condition,

$$\left. \frac{\partial \tau_{dn}}{\partial \hat{Y}} \right|_{\hat{Y}=0} = 0, \quad (2.42)$$

400 which follows from setting  $\hat{Y} = 0$  in (2.14b) and using the no-slip boundary condition  
 401 (2.15a) and the relation (2.38). The system (2.40) is parabolic in the streamwise direction,  
 402 and hence can be solved by a marching procedure in that direction. The system (2.40)  
 403 is truncated by retaining  $N$  number of terms in the Fourier series. The equations were  
 404 discretised using the Crank-Nicolson scheme, which has second-order accuracy in both  
 405 the streamwise and wall-normal directions, and solved in the domain  $\hat{X} \in [-\hat{X}_\infty, \hat{X}_\infty]$   
 406 and  $\hat{Y} \in [0, \hat{Y}_\infty]$ . The far upstream velocities (as  $\hat{X} \rightarrow -\infty$ ) are given by (2.28) for the  
 407 Gaussian streamwise dependence, and (2.34) for the step-like wall shape.

408 The solution procedure is as follows. With the pressure gradient known and the  
 409 nonlinear term estimated using the velocity fields at the three previous  $\hat{X}$ -locations (as  
 410 was done in Ricco *et al.* (2011)), the  $z$ -momentum equation (2.40a) is solved first for the  
 411 spanwise velocity,  $\hat{W}$ , for each  $y$ - $z$  plane slice. The  $x$ -momentum equation (2.40b) with  
 412 (2.42) is then solved for  $\tau_d$ , which is integrated with respect to  $\hat{Y}$  to give the streamwise  
 413 velocity  $\hat{U}_d$  and  $\hat{A}_1$ . Finally, the continuity equation (2.40c) is solved for  $\hat{V}$ . Once the  
 414 velocities are predicted, they are transformed to physical space, where the nonlinear  
 415 terms are evaluated and subsequently transformed once again back to spectral space.  
 416 The aliasing error is eliminated by using the enhanced version of the so-called 2/3-rule  
 417 (Orszag 1971). Due to the nonlinear nature of the problem, an iteration step is needed.  
 418 This consists of repeatedly solving the momentum and continuity equations, updating the  
 419 velocities using an under-relaxation factor of 0.5, and re-evaluating the nonlinear terms.  
 420 The iteration continues until the difference between the consecutive estimates is below a  
 421 specified tolerance of  $10^{-8}$ . Typically, just 1 or 2 iterations sufficed in the region upstream

---

	Roughness 1	Roughness 2	Roughness 3
$f(\hat{X})$	$\exp[-(\hat{X}/d)^2]$	(2.30)	(2.30)
$g(\hat{Z})$	$\frac{1}{2}(1 + \cos(2\pi\hat{Z}/\Lambda))$	$\frac{1}{2}(1 + \cos(2\pi\hat{Z}/\Lambda))$	(2.31)

---

TABLE 1. The three cases considered for the wall shape  $F(\hat{X}, \hat{Z}) = f(\hat{X})g(\hat{Z})$ . The parameters used in the calculations are  $d = 2/3$ ,  $d_x = 0.2$ ,  $l_x = 0.6$ ,  $d_z = 0.45$ ,  $h_z = 0.05$  and  $\Lambda = 1$ .

---

422 of the roughness, elsewhere 5 to 10 iterations were required. The computational domain  
 423 is  $[-5, 5] \times [0, 40]$ , and the numbers of nodes used in the streamwise and wall-normal  
 424 directions are 10000 and 800, respectively. The use of 64 Fourier modes (i.e.  $N = 64$ )  
 425 is found to be sufficient to capture the nonlinear effect. The accuracy and correctness  
 426 of the base flow calculations was supported in several ways. First, the numerical results  
 427 showed a smooth matching with the upstream and far-field asymptotes. Second, the grid  
 428 spacing and the number of Fourier modes used were halved and doubled, respectively, to  
 429 ascertain the convergence and expected accuracy of the results.

### 430 3. Numerical results for the streaky base flow

#### 431 3.1. Lower-deck solution

432 Calculations are performed for three wall shapes (summarised in table 1), namely,

- 433 • roughness 1: Gaussian streamwise and cosine spanwise;
- 434 • roughness 2: step-like streamwise and cosine spanwise;
- 435 • roughness 3: step-like streamwise and hemispherical cap spanwise.

436 Figure 2 shows the profiles of the streamwise velocity deviation  $\hat{U}_d$  along three spanwise  
 437 locations:  $\hat{Z}/\Lambda = 0$  (the centerline of the roughness),  $\hat{Z}/\Lambda = 1/2$ , and  $\hat{Z}/\Lambda = 1/4$ . As  
 438 expected, for all shapes  $\hat{U}_d$  along  $\hat{Z}/\Lambda = 0$  is negative in most of the streamwise region  
 439 due to the flow encountering a wall elevation. For shapes 1 and 2,  $\hat{U}_d$  becomes slightly  
 440 positive just downstream of the peak of the roughness, however this brief increase is  
 441 overturned farther downstream, where  $\hat{U}_d$  decreases again. In contrast, for shape 3,  $\hat{U}_d$   
 442 remains negative along the centerline. For shapes 1 and 2, along  $\hat{Z}/\Lambda = 1/2$  upstream of  
 443 the roughness element there is a velocity excess. This changes downstream of the hump,  
 444 where a velocity deficit forms. The profiles along  $\hat{Z} = 1/2$  for shape 3 are different from  
 445 those for shapes 1 and 2. This is because the flow distortion is concentrated closer to the  
 446 centerline and therefore the velocity deviation is minimal along  $\hat{Z} = 1/2$ . The profiles  
 447 along  $\hat{Z}/\Lambda = 1/4$  for shapes 1, 2 and 3 feature a gradual increase of velocity excess.  
 448 The  $\hat{U}_d$  profiles show that for roughness shapes 1 and 2, high-speed streaks in the region  
 449  $\hat{Z}/\Lambda = \pm 1/4$  and low-speed streaks in the regions  $\hat{Z}/\Lambda = 0$  and  $\hat{Z}/\Lambda = \pm 1/2$  form. For  
 450 shape 3, a low-speed streak can be identified along the centerline. The flow over shape 3  
 451 produces additional streaks, which will be further explored later in this section.

452 A sample of the spanwise velocity profiles along  $\hat{Z}/\Lambda = 1/4$  is displayed in figure  
 453 3. In the region leading up to the hump, at  $\hat{X} = -1, -0.8$  and  $-0.6$ , the spanwise  
 454 velocity is negative. Closer to the roughness maximum (see the velocity profiles at  $\hat{X} =$   
 455  $-0.5, -0.4, -0.3$  and  $-0.1$ ) the flow deforms, giving the spanwise velocity profiles an  
 456 ‘S’-like shape. Downstream of the roughness, at  $\hat{X} = 0.5$ , the spanwise velocity profile

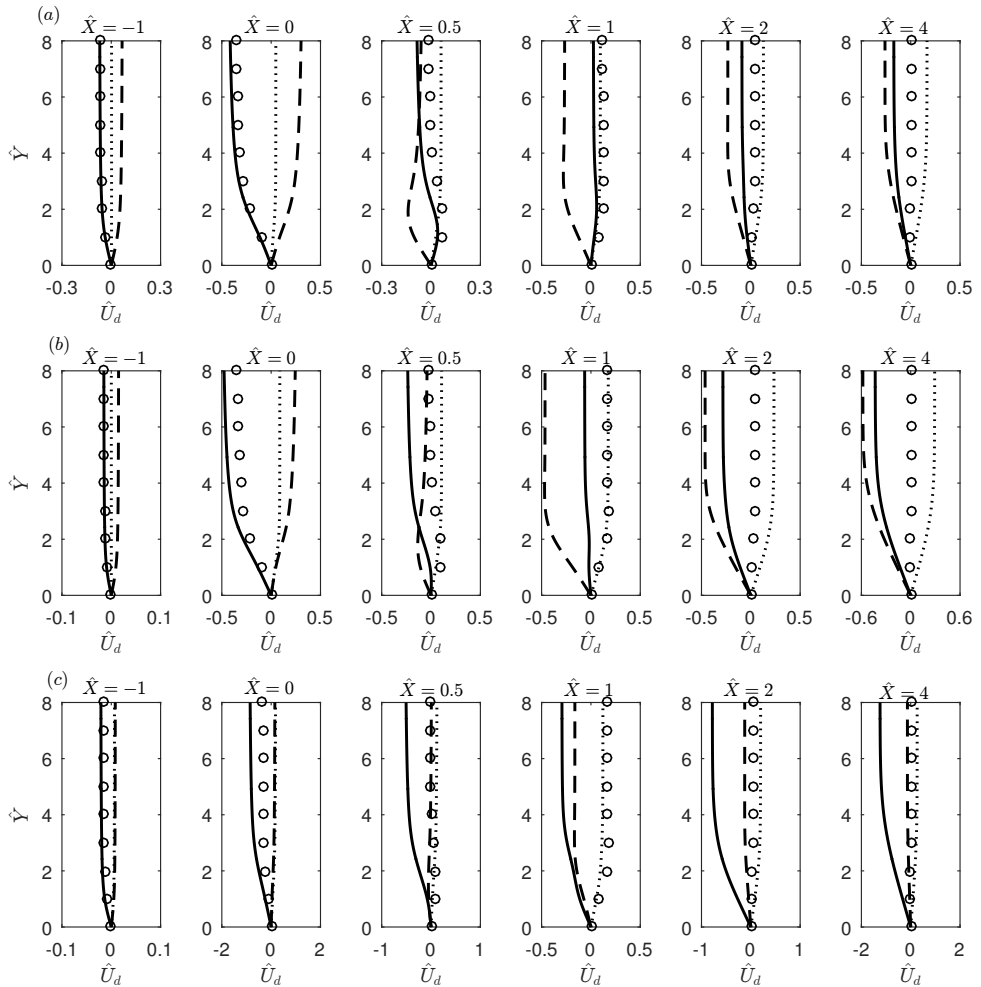


FIGURE 2. Profiles of the velocity deviation  $\hat{U}_d$ , at different streamwise locations for  $\hat{h} = 0.1$ . Solid: along  $\hat{Z}/\Lambda = 0$ . Dashed: along  $\hat{Z}/\Lambda = 1/2$ . Dotted: along  $\hat{Z}/\Lambda = 1/4$ . Marker: linear solution along  $\hat{Z}/\Lambda = 0$ . (a) Roughness shape 1, (b) roughness shape 2, (c) roughness shape 3.

457 is positive everywhere. Farther downstream (e.g. at  $\hat{X} = 0.7, 0.8, 1.2$  and  $2$ ), the flow  
 458 deforms once again and profiles of ‘S’-like shape re-emerge.

459 The spanwise velocity decays downstream of the hump, similarly to the findings of  
 460 Goldstein *et al.* (2016), however, the decay rate is expected to be different in general.  
 461 The spanwise velocity profile for roughness shape 3, at  $\hat{X} = 2$ , is different from the  
 462 respective profiles for shapes 1 and 2. This observation will be discussed further in the  
 463 following sections.

464 The displacement function,  $\hat{A}_1$ , in (2.13) is an important quantity as it plays a crucial  
 465 role in determining the main-deck velocities. An example of the displacement function  
 466 is shown in the left column of figure 4. The contour plots for shapes 1 and 2 are very  
 467 similar, while that for shape 3 is different from the other cases. For shapes 1 and 2  
 468 between  $\hat{X} = -1$  and  $0.5$ , two regions of positive displacement near  $\hat{Z}/\Lambda = \pm 0.5$  and a  
 469 region of negative displacement at  $\hat{Z} = 0$  can be observed. Farther downstream ( $\hat{X} > 0.5$ )

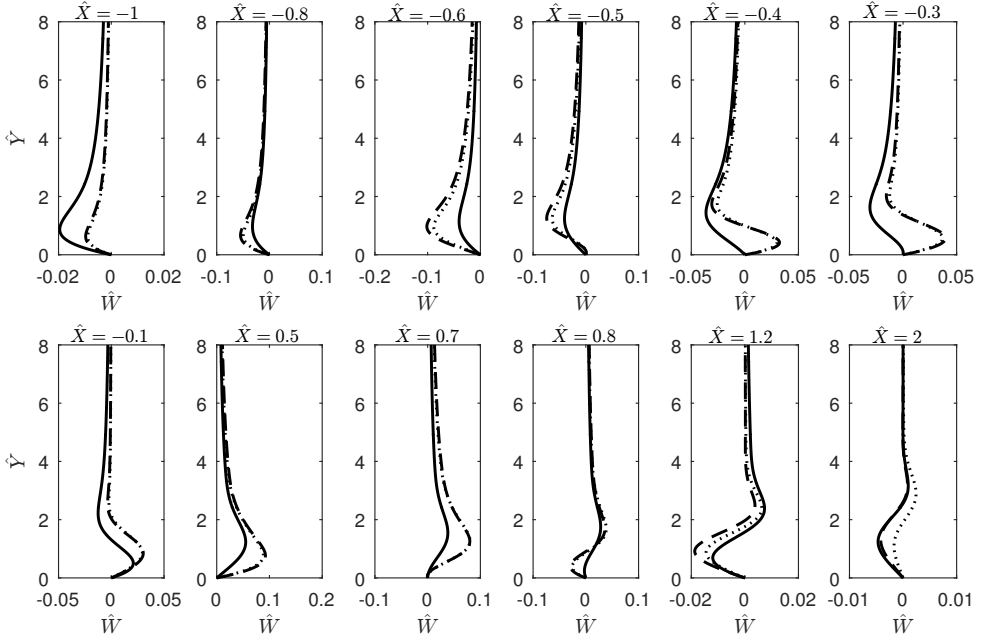


FIGURE 3. Profiles of the spanwise velocity along  $\hat{Z}/\Lambda = 1/4$  for  $\hat{h} = 0.1$ . Solid: roughness shape 1. Dashed: roughness shape 2. Dotted: roughness shape 3.

spanwise alternating positive ( $\hat{Z}/\Lambda = \pm 0.25$ ) and negative ( $\hat{Z}/\Lambda = 0$  and  $\pm 0.5$ ) regions of displacement form. For shape 3, the positive displacement regions between  $\hat{X} = -1$  and 0.5, and the spanwise alternating positive and negative regions downstream ( $\hat{X} > 0.5$ ) are closer to the centerline than for the other two cases. This behaviour can be explained by the fact that shape 3 is narrower than shapes 1 and 2 in the spanwise direction, which causes the flow modulation to concentrate near the centerline.

Our calculations suggest that far downstream the streaks may amplify following algebraic growth,  $\hat{A}_1(\hat{X}) \sim \hat{X}^\gamma$ , where  $\gamma$  is a constant. If this is the case, the asymptotic expansions would break down far downstream, where a new formulation would be needed to describe the flow (cf. Goldstein *et al.* 2010, 2016). A close inspection of the governing equations suggests that  $\gamma = 1/3$  and the solution acquires a self-similar solution, with  $\hat{A}_1$  and the velocities taking the form (Kátai 2020)

$$\begin{aligned} \hat{A}_1(\hat{X}, \hat{Z}) &= \hat{X}^{1/3} \tilde{A}(\hat{Z}), \\ (\hat{U}_d, \hat{V}, \hat{W})(\hat{X}, \hat{Y}, \hat{Z}) &= (\hat{X}^{1/3} \tilde{U}, \hat{X}^{-1/3} \tilde{V}, \hat{X}^{-2/3} \tilde{W})(\hat{\chi}, \hat{Z}), \end{aligned} \quad (3.1)$$

where  $\hat{\chi} \equiv \hat{Y}/\hat{X}^{1/3}$  is the similarity variable, and the governing equations for  $(\tilde{U}, \tilde{V}, \tilde{W})$  turn out to be the same as (5.27)-(5.29) in Goldstein *et al.* (2016) but without the spanwise pressure gradient. The evidence supporting the above downstream asymptote is presented in Figures 5(a) and (b), which display, respectively,  $\hat{X}^{-1/3} \hat{A}_1$  and  $\hat{X}^{-1/3} \hat{U}_d$  versus  $\hat{Y}/\hat{X}^{1/3}$  at several values of  $\hat{X}$ . For each quantity, the curves collapse for sufficiently large  $\hat{X}$ , and the proposed asymptote is reached when  $\hat{X} \approx 5$ . The present regime would cease to be valid farther downstream where the expanding wall layer merges with the main boundary layer; this occurs when  $\epsilon^5 \epsilon_1^{-1/3} \hat{X}^{1/3} = O(\epsilon^4)$ , i.e.  $\hat{X} = O(\epsilon^{-3} \epsilon_1)$ , at which the streaky boundary layer enters a new regime. The development is now over the



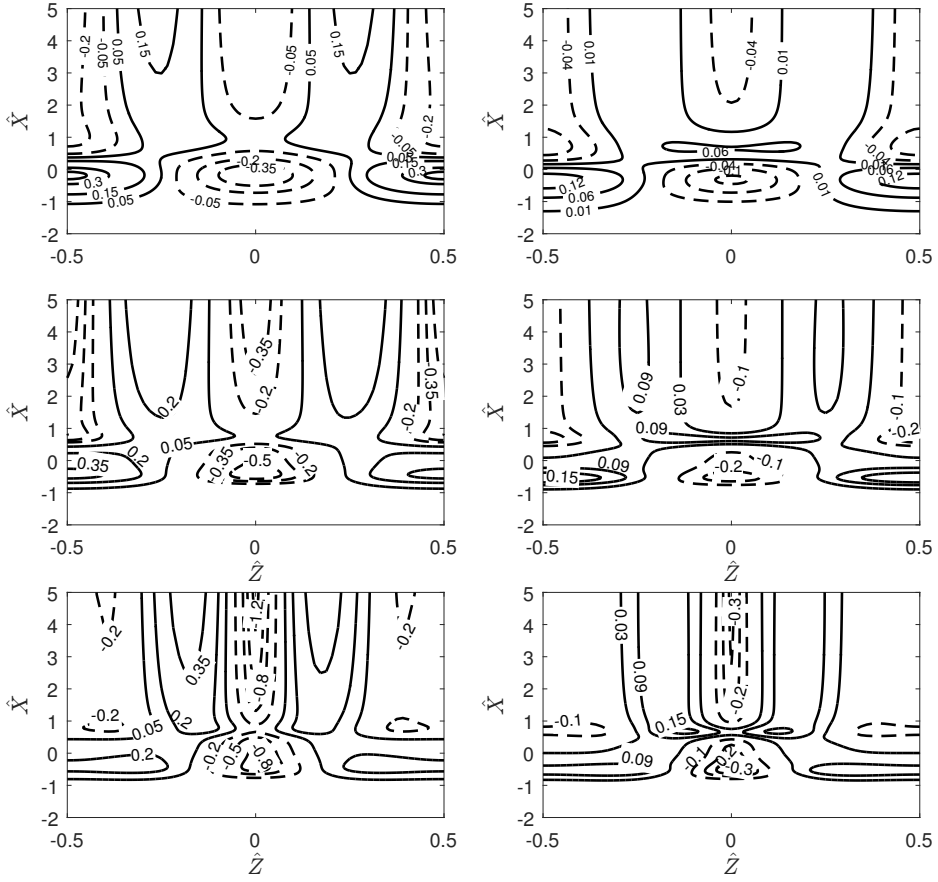


FIGURE 4. Contours of  $\hat{A}_1(\hat{X}, \hat{Z})$  (left column) and of  $(\lambda_u - 1)$  (right column). Top row: roughness 1; middle row: roughness 2; bottom row: roughness 3. All with  $\hat{h} = 0.1$ .

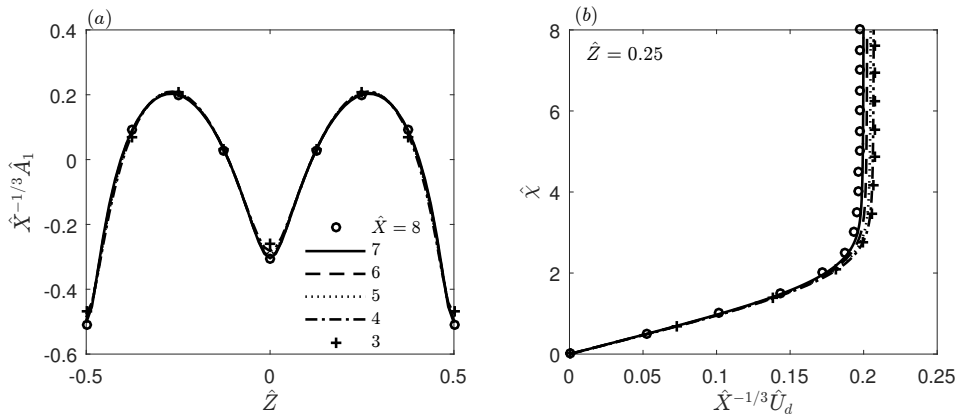


FIGURE 5. Downstream behaviour of (a)  $\hat{A}_1$  and (b)  $\hat{U}_d$  for roughness 1,  $\hat{h} = 0.15$ .

long length scale comparable with  $L$ . The governing equations would remain the same as (2.14), except that the pressure gradient drops out,  $\hat{X}$  is replaced by  $\check{X} \equiv (\epsilon^3/\epsilon_1)\hat{X}$  and  $\hat{Y}$  by  $\check{Y} \equiv (\epsilon/\epsilon_1^{1/3})\hat{Y}$ . The main differences are: (a) the far-field boundary conditions will be modified, and (b) a composite solution must be constructed from (3.1) and its counterpart in the main layer to provide the ‘initial’ condition for the new regime. Now without any external forcing, the streaks would ultimately decay. A detailed study of this final regime is left for the future.

Another important quantity is the wall shear,

$$\lambda_u(\hat{X}, \hat{Z}) = 1 + \tau_d(\hat{X}, 0, \hat{Z}), \quad (3.2)$$

which controls the linear stability of the streaky flow, as will be shown in §4. The right column of figure 4 displays contours of  $(\lambda_u - 1)$ . The streamwise evolution of the wall shear follows a similar trend to that of the displacement function. Again, for shapes 1 and 2, positive (near  $\hat{Z}/\Lambda = \pm 0.5$ ) and negative (near  $\hat{Z} = 0$ ) regions of  $(\lambda_u - 1)$  emerge between  $\hat{X} = -1$  and 0.5. Also, in the downstream region ( $\hat{X} > 0.5$ ), there arise spanwise alternating positive ( $\hat{Z}/\Lambda = \pm 0.25$ ) and negative ( $\hat{Z}/\Lambda = 0$  and  $\pm 0.5$ ) streaky regions of  $(\lambda_u - 1)$ . Similar observations can be made for shape 3 (the bottom right plot of figure 4) with the difference that the positive regions of  $(\lambda_u - 1)$  between  $\hat{X} = -1$  and 0.5, and the spanwise alternating positive and negative regions downstream ( $\hat{X} > 0.5$ ) are closer to the centerline than for the other two cases. This is again due to the fact that shape 3 is more compact in the spanwise direction. For the same roughness height, the largest  $|\lambda_u - 1|$  is produced by shape 3.

### 3.2. Parameters pertaining to the experiments of Downs & Fransson (2014)

The most relevant experiment, with which our theoretical results will be compared, is that of Downs & Fransson (2014). Table 2 shows the key parameters that can be drawn from their study. The distance between the leading edge and the roughness was relatively short (around 300 mm) when compared to the roughness length (250 mm). The streamwise and spanwise lengths of the roughness of the present study are, however, in good agreement with those in the experiment of Downs & Fransson (2014).

The roughness height in the experiment is almost 2-3 times those used in our numerical calculations. Further increasing the roughness height in the calculations resulted in a zero wall shear, which signaled flow separation and rendered the numerical algorithm inadequate. As we will see in the following sections, the geometry of the roughness elements has a great impact on the location of flow separation. For example, for roughness shape 2 with  $\hat{h} = 0.15$ , the flow does not separate in the domain examined ( $\hat{X} \in [-5, 5]$ ) whilst it does for roughness shape 3. The vanishing wall shear occurs when the roughness height exceeds a critical value  $\hat{h}_c$ , and so the separation is of marginal type (cf. Ruban 1982; Stewartson *et al.* 1982). The classical boundary-layer solution is expected to remain valid except in a small neighbourhood of the point of zero wall shear, where the self-induced pressure may be important. On the other hand, the separation, caused by the spanwise pressure gradient, is of the so-called ‘collision type’, probably akin to that described in Stewartson & Simpson (1982). An appropriate theory for such a form of marginal separation would differ from that of Brown (1985) and should be pursued in the future. The separating boundary layer would acquire a shorter streamwise length scale, and so the streamwise diffusion becomes enhanced, but is unlikely, as in Ruban (1982) and Brown (1985), to appear at leading order. The present paper focuses on roughness heights less than  $\hat{h}_c$ , only for which stabilization is likely in practice.

Normalised Parameters	Downs & Fransson (2014)	Present study
$\hat{h} = \epsilon^{-5} \epsilon_1^{2/3} \lambda_B^{3/4} h^*/L$	0.5	0 - 0.2
$\Lambda = \epsilon^{-3} \lambda_B^{5/4} \Lambda^*/L$	1.1	1
$L_x = \epsilon^{-3} \epsilon_1 \lambda_B^{5/4} L_x^*/L$	1.1	$\approx 1.2$
$\epsilon_1 = \Lambda^*/L_x^*$	0.06	0.06
$\epsilon = R^{-1/8}$	$\approx 0.2$	0.2
$F_r = 10^6 \epsilon^6 \lambda_B^{3/2} \omega$	100	61 - 122
$\omega$	$\approx 8.2$	5 - 10

TABLE 2. The non-dimensional parameters that pertain to the experiment of Downs & Fransson (2014) and those used in our calculations. The distance to the leading edge,  $L = 425$  mm, dimensional roughness height,  $h^* = 1$  mm, spanwise spacing,  $\Lambda^* = 15$  mm, roughness length,  $L_x^* = 250$  mm, and the dimensionless frequency  $F_r = 2\pi\nu f^* \times 10^6/U_\infty^* = 100$ , where  $f^*$  and  $\omega$  denote the dimensional and normalised frequencies of the instability wave.

### 3.3. Streaky base flow

Figures 6-7 display contours in the  $y - z$  plane of the composite streamwise velocity  $u^c$  (see (2.37)) and its deviation from  $U_B$  for roughness shapes 1 and 2. The contours at different streamwise locations show how the roughness elements produce the streaky base flow, which may stabilise the flow and potentially delay transition to turbulence. The flow characteristics for roughness shapes 1 and 2 are qualitatively similar to those found in the experiments of Fransson *et al.* (2004) and Downs & Fransson (2014).

As figures 6-7 illustrate, initially ( $x^*/L = 0.72$  and 1) a velocity deficit arises along the centerline of the roughness ( $\hat{Z} = 0$ ) and a region of velocity excess appears on either side of the roughness ( $\hat{Z}/\Lambda = \pm 0.5$ ) near the wall. However, this changes just after  $x^*/L = 1$ . Downstream of the hump ( $x^*/L = 1.11, 1.28$ ), the high-speed streaks coalesce into a single streak. In the same streamwise region, the low-speed streaks at  $\hat{Z} = \pm 0.5$  descend towards the wall, along with the high-speed fluid at  $\hat{Z} = 0$ , as a result of which the region of velocity deficit develops into one of excess. The latter elongates in the spanwise direction and then splits into two high-speed streaks while a low-speed streak forms between them. As a result, the streak structure consists of alternating low- and high-speed regions.

The contour plots of figures 6 and 7 look very similar despite the fact that they pertain to roughness with different streamwise shapes but the same spanwise shape, indicating that the latter might have a greater effect on the form of the induced streaks. This suggestion is supported by comparing figures 6 and 7 with figure 8 for shape 3, where the flow modulation is concentrated about the centre of the hump, and the central velocity deficit region persists all the way from upstream to downstream locations. It can also be observed that for a given roughness height the largest difference in high- and low-speed streaks arises for roughness shape 3. Velocity excess and deficit as large as 0.15 and -0.24, respectively, can occur downstream of the roughness (see figure 8), much stronger than those for the other two cases (see figures 6 and 7).

Naturally, the characteristics shown in figure 2 feature in figures 6-8 as well, that is, the streamwise velocity starts upstream with a velocity deficit along the centerline of the roughness element together with regions of velocity excess along  $\hat{Z}/\Lambda = \pm 1/2$  (around  $\hat{Z}/\Lambda = \pm 0.2$  for shape 3). This changes as the fluid flows over the peak of the roughness element. The high- and low-speed streaks evolve into, respectively, low-

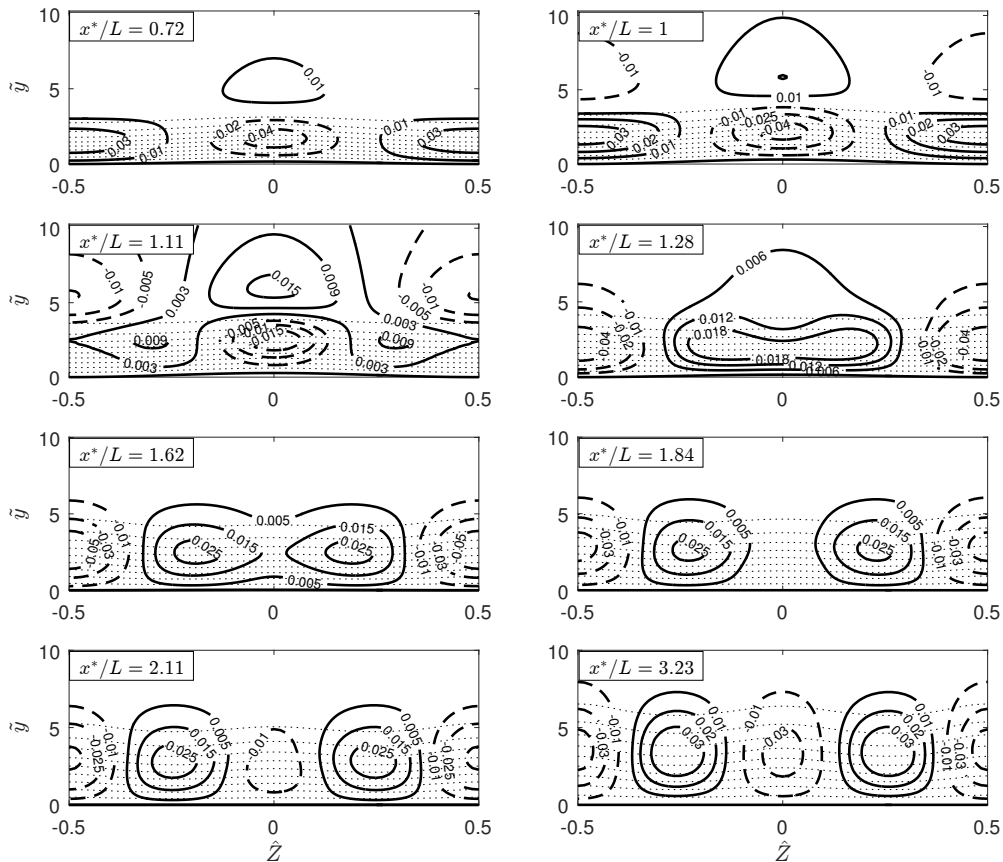


FIGURE 6. Streaky base flow as shown by contours of the composite streamwise velocity  $u^c$  and  $u^d \equiv u^c - U_B$ , the deviation from the Blasius flow for roughness shape 1. Dotted lines: contours of  $u^c$  with an increment of 0.1. Solid lines:  $u^d > 0$ ; dashed lines:  $u^d < 0$ . Parameters:  $\epsilon = 0.2$ ,  $\epsilon_1 = 0.06$  and  $\hat{h} = 0.1$ .

562 and high-speed streaks. Interestingly, for shapes 1 and 2, the central high-speed streak  
 563 splits into two, and a low-speed streak is formed between these two newly formed high-  
 564 speed streaks. For shape 3, however, the central low-speed streak survives throughout  
 565 the domain. In figure 8a of Downs & Fransson (2014), velocity deficits are observed  
 566 downstream of the roughness elements along the centreline ( $\hat{Z} = 0$ ) and in the valleys  
 567 ( $\hat{Z} = \pm 0.5$ ). In addition, high-speed streaks are observed between the low-speed streaks  
 568 near  $\hat{Z} = \pm 0.25$ . The present calculations showed that a single hump produced four  
 569 distinct streaks downstream of the elements. For future work it could be interesting to  
 570 investigate the effect of even narrower spanwise roughness shapes.

571 There are many ways to quantify and compare various streaky flows. A common  
 572 measure, with which streak instability correlates, is the integral streak amplitude, defined  
 573 as (Shahinfar *et al.* 2013)

$$A_{ST}(x) = \frac{1}{\Lambda} \int_{-\Lambda/2}^{\Lambda/2} \int_0^\infty |u(x, \eta, \hat{Z}) - u^{\hat{Z}}(x, \eta)| d\eta d\hat{Z}, \quad (3.3)$$

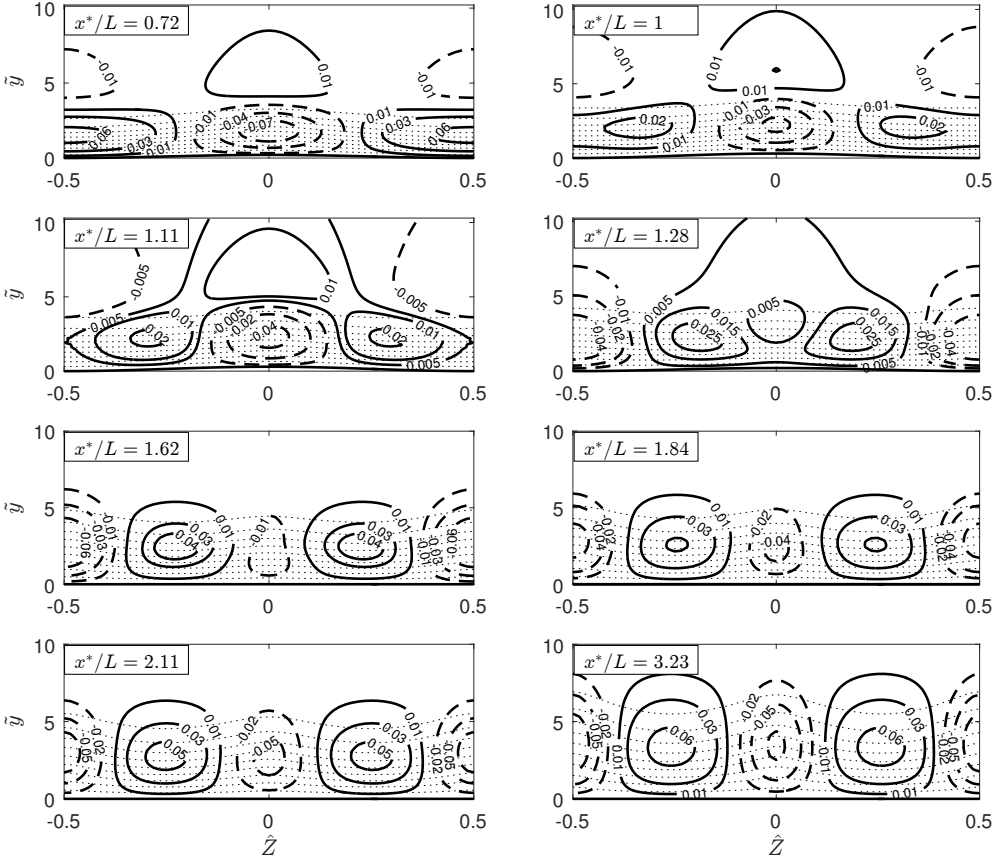


FIGURE 7. Streaky base flow as shown by contours of the composite streamwise velocity  $u^c$  and  $u^d \equiv u^c - U_B$ , the deviation from the Blasius flow for roughness shape 2. Dotted lines: contours of  $u^c$  with an increment of 0.1. Solid lines:  $u^d > 0$ ; dashed lines:  $u^d < 0$ . Parameters:  $\epsilon = 0.2$ ,  $\epsilon_1 = 0.06$  and  $\hat{h} = 0.1$ .

574 where the superscript  $\hat{Z}$  indicates the spanwise averaged quantity

$$u^{\hat{Z}}(\hat{X}, \hat{Y}) = \frac{1}{\Lambda} \int_{-\Lambda/2}^{\Lambda/2} u(\hat{X}, \hat{Y}, \hat{Z}) d\hat{Z}. \quad (3.4)$$

575 Using the composite solution (2.37), we obtain the integral streak amplitude:

$$A_{ST}(x) = \lambda_B^{1/4} R_x^{-1/8} \epsilon_1^{-1/3} \frac{1}{\Lambda} \int_{-\Lambda/2}^{\Lambda/2} \int_0^\infty \left| \hat{U}_d(\hat{X}, \hat{Y}, \hat{Z}) - \hat{U}_d^{\hat{Z}}(\hat{X}, \hat{Y}) \right. \\ \left. + (\hat{A}_1(\hat{X}, \hat{Z}) - \hat{A}_1^{\hat{Z}}(\hat{X})) (U_B'(\hat{y})/\lambda_B - 1) \right| d\eta d\hat{Z}. \quad (3.5)$$

576 Streak amplitudes for the three wall shapes are shown in figure 9. Naturally, higher  
577 roughness elements produce larger streak amplitudes, but the streak amplitude depends  
578 on the roughness geometry as well. The amplitude generated by roughness shape 3 is  
579 higher than those for the other two cases. For shape 3 with  $\hat{h} = 0.15$ , a reverse flow is  
580 observed just upstream of the roughness element.

581 Another key quantity characterising the streaky flow is the displacement thickness  $\delta^*$ ,

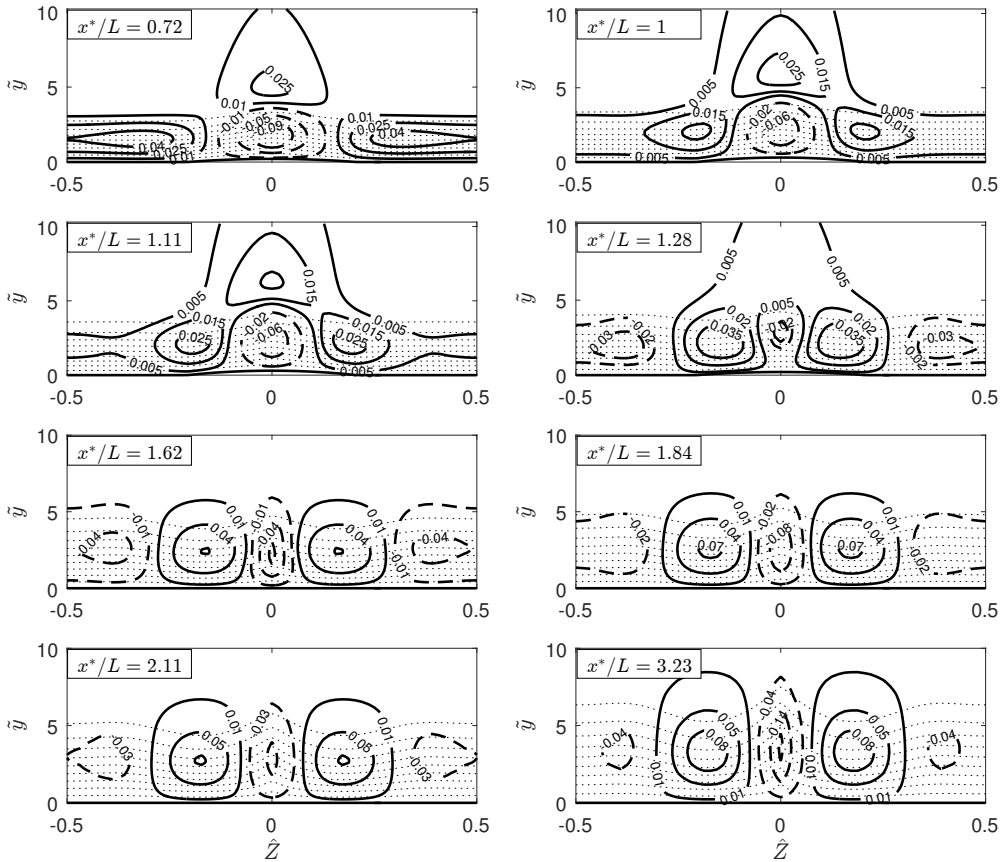


FIGURE 8. Streaky base flow as shown by contours of the composite streamwise velocity  $u^c$  and  $u^d \equiv u^c - U_B$ , the deviation from the Blasius flow for roughness shape 3. Dotted lines: contours of  $u^c$  with an increment of 0.1. Solid lines:  $u^d > 0$ ; dashed lines:  $u^d < 0$ . Parameters:  $\epsilon = 0.2$ ,  $\epsilon_1 = 0.06$  and  $\hat{h} = 0.1$ .

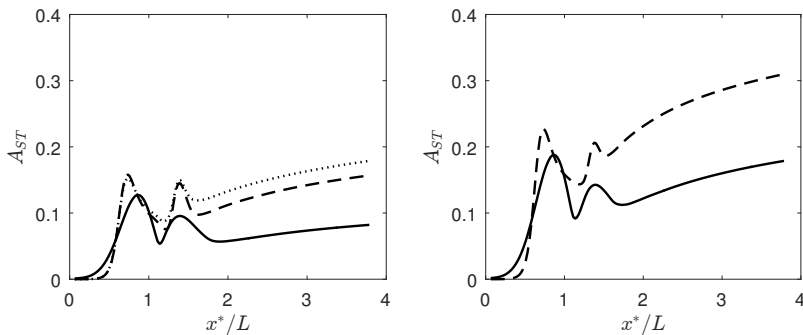


FIGURE 9. The streamwise development of the streak amplitude  $A_{ST}$ . Solid lines: roughness shape 1. Dashed line: roughness shape 2. Dotted line: roughness shape 3. Left:  $\hat{h} = 0.1$ . Right:  $\hat{h} = 0.15$ . Parameters  $\epsilon = 0.2$ ,  $\epsilon_1 = 0.06$  and  $\Lambda = 1$ .

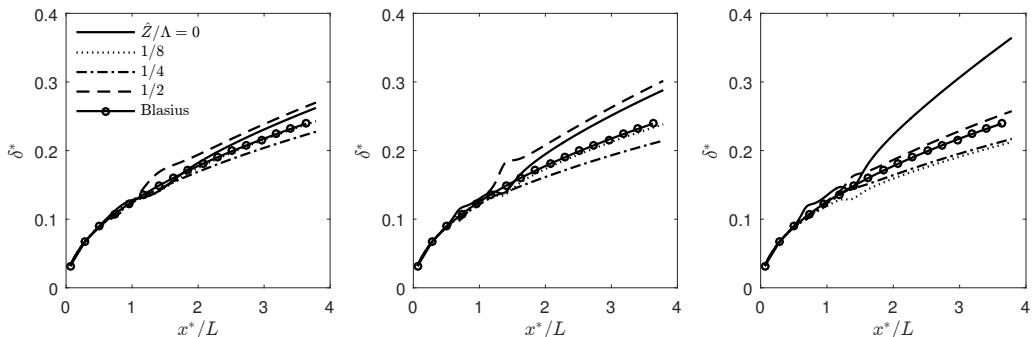


FIGURE 10. The streamwise distribution of the displacement thickness  $\delta^*$  at different spanwise positions. Left: roughness shape 1. Middle: roughness shape 2. Right: roughness shape 3. The parameters are  $\hat{h} = 0.1$ ,  $\epsilon = 0.2$ ,  $\epsilon_1 = 0.06$  and  $\Lambda = 1$ .

582 which is defined as

$$\delta^*(x, z) = \int_0^\infty [1 - u(x, y, z)] dy^* = R^{-1/2} (x^* L)^{1/2} \int_0^\infty [1 - u(x, \eta, z)] d\eta, \quad (3.6)$$

583 where  $u$  is the nondimensional streamwise velocity, for the present calculations the  
 584 composite solution  $u^c$  was used. The development of the displacement thickness at  
 585 representative spanwise locations are displayed in figure 10 for the three roughness shapes.  
 586 The results for shapes 1 and 2 show many similarities. The displacement thickness is the  
 587 largest in the low-speed regions (valleys) along  $\hat{Z} = \pm 1/2$ . The second largest displacement  
 588 thickness is along the centerline ( $\hat{Z} = 0$ ). For roughness shape 3, the largest displacement  
 589 thickness downstream occurs along the centerline ( $\hat{Z} = 0$ ); see the right part of figure 10.  
 590 The displacement thickness along the valley ( $\hat{Z}/\Lambda = 1/2$ ) is close to that of the Blasius  
 591 flow. This is because the distortion concentrates along  $\hat{Z} = 0$ . In general, roughness shape  
 592 3 causes a greater disruption to the boundary layer, and for the same height ( $\hat{h} = 0.15$ )  
 593 the flow experiences reversal, which does not occur in the other two cases.

594 Our calculations have already covered rather an extended wake region, extending nearly  
 595 4 times the distance between the leading edge and the roughness centre (as figure 10  
 596 indicates). In this region, the streak amplitude increases but rather moderately without  
 597 causing an order-of-magnitude change, and thus the solution in the current asymptotic  
 598 regime is expected to be valid and suitable for the stability calculation. Due to the rather  
 599 slow (i.e.  $\hat{X}^{1/3}$ ) algebraic growth, the new asymptotic regime would commence only at  
 600 very distant locations. The precise locations and quantitative effects of the new regime  
 601 require further study.

#### 602 4. Linear stability analysis of the streaky boundary layer

603 The linear stability of the streaky boundary layer resulting from three-dimensional  
 604 arrays of roughness elements has been analysed by Piot *et al.* (2008) and Siconolfi  
 605 *et al.* (2015), who solved the viscous bi-global eigenvalue problem resulting from the  
 606 linearised unsteady N–S equations. An important point to note is that insofar as the  
 607 streaks play a stabilising role, the instability must be of viscous nature, ceasing to  
 608 exist if the viscous terms are neglected. This is a rather subtle difference from the  
 609 essentially inviscid instability of the streaks in bypass transition or Görtler vortices in  
 610 the boundary layer over a concave wall (Hall & Horseman 1991; Li & Malik 1995). In  
 611 this section, the rather fundamental viscous streak instability will be analysed in the

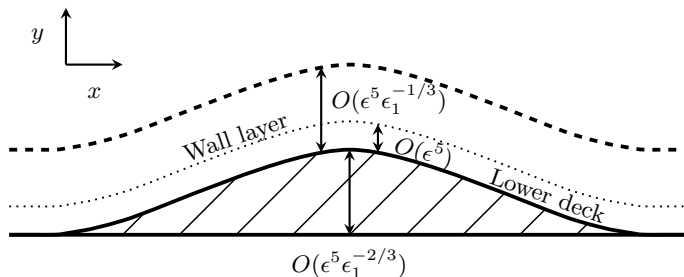


FIGURE 11. A sketch of the asymptotic structure: the viscous wall layer (dashed line) for the roughness-induced mean-flow distortion and the lower deck for the secondary instability (dotted line).

high-Reynolds-number limit. The asymptotic analysis will reduce the viscous bi-global stability problem to a much simpler one-dimensional problem, and allow us to probe into the essential underlying physics. In the finite-Reynolds-number formulation, the viscous term appears to be  $O(R^{-1/2})$ , while the effect of non-parallelism is of order  $\epsilon_1$ , the ratio of the streamwise length scale of the instability to that of the streaky flow, which is at least as large as  $O(R^{-1/2})$ , and yet non-parallelism is neglected in favour of the viscous effect. The justification for this, i.e. the dominance of the viscous effect and the relatively minor role of non-parallelism, will transpire in the present high-Reynolds-number framework.

In order to fix the idea, the stability analysis will be performed using the asymptotic solution for the streaky base flow, although the analysis can, with minor adjustments, be applied to general streaky flows (e.g. those obtained by solving the steady N–S equations) provided that the streaks have the required streamwise and spanwise length scales (2.11).

In the absence of roughness, it is well known that the lower-branch instability of the boundary layer is governed by the standard triple deck structure (Lin 1945; Smith 1979*b*). The instability modes have characteristic frequency of  $O(\epsilon^{-2}U_\infty/L)$ , streamwise and spanwise wavelength of  $O(\epsilon^{-3}L)$ , much greater than the local boundary-layer thickness. The scalings remain intact for the roughness considered, and thus the time variable and spatial coordinates are,

$$t = \epsilon^2 T = \epsilon^2 \lambda_B^{-3/4} \hat{T}, \quad x = \epsilon^3 X = \epsilon^3 \lambda_B^{-5/4} X^\dagger, \quad z = \epsilon^3 Z = \epsilon^3 \lambda_B^{-5/4} \hat{Z}, \quad (4.1a - c)$$

where  $\hat{T} = O(1)$ ,  $X^\dagger = O(1)$ ,  $\hat{Z} = O(1)$  and  $\lambda_B = 0.33206$  as usual. The instability modes are proportional to

$$E = \exp[i(\alpha_o x - \omega_o t)] = \exp[i(\alpha X^\dagger - \omega \hat{T})], \quad (4.2)$$

where the angular frequency,  $\omega_o$ , and wavenumber,  $\alpha_o$ , are of  $O(\epsilon^{-2})$  and  $O(\epsilon^{-3})$  respectively. Hence, the normalised frequency and wavenumber are,

$$\omega = \lambda_B^{-3/2} \epsilon^2 \omega_o = O(1), \quad \alpha = \lambda_B^{-5/4} \epsilon^3 \alpha_o = O(1), \quad (4.3)$$

as in the classical triple-deck scaling. The eigenfunctions depend on the wall-normal and spanwise coordinates. The ensuing analysis will involve quantities that have been rescaled with respect to  $\lambda_B$ .

#### 4.1. Lower Deck

The lower deck for the instability has  $O(\epsilon^{-5}L)$  width. It is adjacent to the curved surface of the roughness, and is embedded within the much thicker wall layer; the flow structure is shown in figure 11. Thus we introduce the local transverse coordinate  $Y^\dagger$



635 through

$$y - \epsilon^5 h F = \epsilon^5 \tilde{Y} = \epsilon^5 \lambda_B^{-3/4} Y^\dagger, \quad (4.4)$$

636 as in (2.9). Correspondingly, the wall-normal velocities in the lower deck are subject to  
637 the Prandtl transposition, similarly to (2.9).

638 The velocities and pressure including the disturbance expand as,

$$u = \epsilon U = \epsilon \epsilon_1^{-1/3} \lambda_B^{1/4} U_b + \epsilon \epsilon_d \lambda_B^{1/4} [U_1 + \dots] E, \quad (4.5a)$$

$$v = \epsilon^3 V = \epsilon^3 \epsilon_1^{1/3} \lambda_B^{3/4} V_b + \epsilon^3 \epsilon_d \lambda_B^{3/4} [V_1 + \dots] E, \quad (4.5b)$$

$$w = \epsilon W = \epsilon \epsilon_1^{2/3} \lambda_B^{1/4} W_b + \epsilon \epsilon_d \lambda_B^{1/4} [W_1 + \dots] E, \quad (4.5c)$$

$$p = \epsilon^2 P = \epsilon^2 \epsilon_1^{4/3} \lambda_B^{1/2} P_b + \epsilon^2 \epsilon_d \lambda_B^{1/2} [P_1 + \dots] E, \quad (4.5d)$$

where  $\epsilon_d \ll 1$  represents the amplitude of the instability mode. The rescaled base-flow field  $(U_b, V_b, W_b, P_b)$  is calculated numerically in §3, and it varies slowly on a scale greater than the classical triple-deck scale because the roughness is elongated in the streamwise direction. Since the present lower deck for the instability modes is much thinner than that for the steady streaky base flow, the velocities of the latter can be approximated using a Taylor series expansion about the wall as

$$U_b \sim \epsilon_1^{1/3} \lambda_u Y^\dagger + \dots, \quad V_b \sim \epsilon_1^{2/3} \lambda_v Y^{\dagger 2} + \dots, \quad W_b \sim \epsilon_1^{1/3} \lambda_w Y^\dagger + \dots, \quad (4.6a - c)$$

639 where  $\lambda_u$  and  $\lambda_w$  are the streamwise and spanwise wall shears, normalised by  $\lambda_B$  and  
640  $\lambda_v = -(\partial \lambda_u / \partial \hat{X} + \partial \lambda_w / \partial \hat{Z}) / 2$ .

641 Substituting the expansion (4.5) with (4.6) into the N-S equations, we obtain the  
642 continuity, the  $x$ -, and  $z$ -momentum equations,

$$i\alpha U_1 + \frac{\partial V_1}{\partial Y^\dagger} + \frac{\partial W_1}{\partial \hat{Z}} = 0, \quad (4.7a)$$

643

$$-i\omega U_1 + i\alpha \lambda_u Y^\dagger U_1 + \lambda_u V_1 + \lambda_{u\hat{Z}} Y^\dagger W_1 = -i\alpha P_1 + \frac{\partial^2 U_1}{\partial Y^{\dagger 2}}, \quad (4.7b)$$

644

$$-i\omega W_1 + i\alpha \lambda_u Y^\dagger W_1 = -\frac{\partial P_1}{\partial \hat{Z}} + \frac{\partial^2 W_1}{\partial Y^{\dagger 2}}, \quad (4.7c)$$

645 while the  $y$ -momentum equation gives  $\partial P_1 / \partial Y^\dagger = 0$ , so that  $P_1$  is a function of  $\hat{Z}$   
646 only, where  $\lambda_{u\hat{Z}} = \partial \lambda_u / \partial \hat{Z}$  represents the spanwise derivative of the wall shear  $\lambda_u$ .  
647 As with the T-S instability (Lin 1945; Smith 1979b), the viscous diffusion in the wall-  
648 normal direction is obviously a leading-order effect, whereas the streamwise and spanwise  
649 diffusions have been neglected because they are much smaller by a factor of  $O(R^{-1/2})$  due  
650 to the long wavelength nature of the stability; for the same reason removal of these two  
651 terms from the Orr-Sommerfeld equation was found to cause a minor quantitative error  
652 (Govindarajan 1997). The non-parallelism is now associated with the slow streamwise  
653 variation  $\partial \lambda_u / \partial X^\dagger$ , and an inspection of the terms in the disturbance momentum  
654 equations indicates that this effect contributes an  $O(\epsilon_1)$  correction, which is negligible  
655 for an elongated roughness. It follows that a local linear stability is not applicable when  
656 the aspect ratio  $\epsilon_1 = O(1)$ , in which case an extension of the local scattering theory (Wu  
657 & Dong 2016) is required to account for the impact of the roughness on transition.

## 4.2. Main Deck

In the main deck, where  $y = \epsilon^4 \lambda_B^{-3/4} \check{y}$  with  $\check{y} = O(1)$ , the velocities and pressure including the disturbance expand as:

$$\{u, v, w, p\} = \left\{ \lambda_B^{1/4} u_b, \epsilon^2 \epsilon_1^{1/3} \lambda_B^{3/4} v_b, \epsilon^2 \epsilon_1 \lambda_B^{1/4} w_b, \epsilon^2 \epsilon_1^{4/3} \lambda_B^{1/2} P_b \right\} \\ + \epsilon \epsilon_d \{ \lambda_B^{1/4} u_1, \lambda_B^{3/4} \epsilon v_1, \epsilon \lambda_B^{1/4} w_1, \epsilon \lambda_B^{1/2} p_1 \} E + \dots, \quad (4.8)$$

where the quantities with subscript  $b$  referring to those of the base flow consisting of the Blasius solution and the distortion due to the elongated surface roughness elements. The equations governing the disturbance follow from substituting (4.8) into the N-S equations, and they have the leading-order solution,

$$u_1 = A_1 \frac{\partial u_b}{\partial \check{y}}, \quad v_1 = -i\alpha A_1 u_b, \quad w_1 = -\frac{1}{i\alpha u_b} \frac{\partial p_1}{\partial \hat{Z}}, \quad p_1 = P_1(\hat{Z}). \quad (4.9a - d)$$

## 4.3. Upper Deck

In the upper deck, where  $y^\dagger = \epsilon^{-3} \lambda_B^{5/4} y = O(1)$ , the disturbed velocities and pressure expand in the form,

$$\{u, v, w, p\} = \left\{ 1, O(\epsilon^2 \epsilon_1^{1/3}), O(\epsilon^2 \epsilon_1), O(\epsilon^2 \epsilon_1^{4/3}) \right\} + \epsilon^2 \epsilon_d \lambda_B^{1/2} \{u^\dagger, v^\dagger, w^\dagger, p^\dagger\} E + \dots, \quad (4.10)$$

where the base flow is virtually the uniform stream. Substituting the expansion (4.10) into the N-S equations, we obtain at leading order,

$$i\alpha u^\dagger + \frac{\partial v^\dagger}{\partial y^\dagger} + \frac{\partial w^\dagger}{\partial \hat{Z}} = 0, \quad u^\dagger = -p^\dagger, \quad i\alpha v^\dagger = -\frac{\partial p^\dagger}{\partial y^\dagger}, \quad i\alpha w^\dagger = -\frac{\partial p^\dagger}{\partial \hat{Z}}. \quad (4.11a - d)$$

Elimination of the velocities leads to the equation for the pressure in the upper deck,

$$-\alpha^2 p^\dagger + \left( \frac{\partial^2}{\partial y^{\dagger 2}} + \frac{\partial^2}{\partial \hat{Z}^2} \right) p^\dagger = 0, \quad (4.12)$$

which will be considered along with the lower-deck equations in §4.5.

## 4.4. The lower-deck solutions

The lower-deck equations (4.7) are similar to those formulated by Smith (1979a), which we shall follow to solve for the lower-deck disturbance velocities and pressure.

The equation governing the spanwise disturbance velocity (4.7c) is solved first using the change of variable

$$\xi = (i\lambda_u \alpha)^{1/3} Y^\dagger + \xi_0, \quad \xi_0(\hat{Z}) = -i\omega (i\lambda_u \alpha)^{-2/3}. \quad (4.13)$$

with the no-slip and matching conditions

$$W_1|_{\xi=\xi_0} = 0 \quad \text{and} \quad W_1 \rightarrow -\frac{\partial P_1 / \partial \hat{Z}}{i\alpha \lambda_u \xi} \quad \text{as} \quad \xi \rightarrow \infty. \quad (4.14)$$

The solution  $W_1$  is found as

$$W_1 = \frac{\pi P_1 \hat{Z}}{(i\alpha \lambda_u)^{2/3}} \left( \frac{\text{Gi}(\xi_0)}{\text{Ai}(\xi_0)} \text{Ai}(\xi) - \text{Gi}(\xi) \right). \quad (4.15)$$

672 We differentiate (4.7b) with respect to  $Y^\dagger$  to eliminate the pressure, and use the  
 673 continuity equation (4.7a) in the resulting equation to eliminate  $V_1$ . Finally, using the  
 674 change of variable (4.13), we obtain the equation for  $U_1$ ,

$$U_{1\xi\xi\xi} - \xi U_{1\xi} = -\frac{1}{i\alpha} \frac{\partial W_1}{\partial \hat{Z}} + \frac{\partial \lambda_u / \partial \hat{Z}}{i\alpha \lambda_u} \left( \xi + \frac{(i\alpha \lambda_u)^{1/3} \omega}{\alpha \lambda_u} \right) \frac{\partial W_1}{\partial \xi} + \frac{\partial \lambda_u / \partial \hat{Z}}{i\alpha \lambda_u} W_1, \quad (4.16)$$

675 with the boundary and matching conditions being expressed as

$$U_1 \Big|_{\xi=\xi_0} = 0, \quad \frac{\partial^2 U_1}{\partial \xi^2} \Big|_{\xi=\xi_0} = \frac{i\alpha P_1}{(i\alpha \lambda_u)^{2/3}} \quad \text{and} \quad U_1 \Big|_{\xi \rightarrow \infty} \rightarrow u_1 \Big|_{\tilde{y}=0} = \lambda_u A_1. \quad (4.17)$$

676 By using the expression for  $W_1$ , (4.15), the solution to (4.16) is found as

$$U_1 = B_1 \int_{\xi_0}^{\xi} \text{Ai}(t) dt + \left( \psi_1 - \frac{3}{4} \phi_1 \right) \text{Ai}(\xi) + \left( \psi_2 - \frac{3}{4} \phi_2 \right) \text{Gi}(\xi) + \frac{\phi_1}{4} \xi \text{Ai}'(\xi) + \frac{\phi_2}{4} \xi \text{Gi}'(\xi) \\ - \left( \psi_1 - \frac{3}{4} \phi_1 \right) \text{Ai}(\xi_0) - \left( \psi_2 - \frac{3}{4} \phi_2 \right) \text{Gi}(\xi_0) - \frac{\phi_1}{4} \xi_0 \text{Ai}'(\xi_0) - \frac{\phi_2}{4} \xi_0 \text{Gi}'(\xi_0), \quad (4.18)$$

677 where the expressions for  $B_1$ ,  $\psi_1$ ,  $\psi_2$ ,  $\phi_1$  and  $\phi_2$  are given in the appendix A. Use of the  
 678 matching condition for  $U_1$  in (4.17) yields the equation for the pressure,

$$\left( \frac{\partial^2}{\partial \hat{Z}^2} - \frac{\lambda_u \hat{Z}}{\lambda_u} \mathcal{G}(\xi_0) \frac{\partial}{\partial \hat{Z}} - \alpha^2 \right) P_1 - \frac{(i\alpha \lambda_u)^{5/3} \text{Ai}'(\xi_0)}{\kappa(\xi_0)} A_1 = 0, \quad (4.19)$$

679 where we have put

$$\mathcal{G}(\xi_0) = \frac{3}{2} + \frac{\xi_0}{2\text{Ai}(\xi_0)} (\xi_0 \kappa(\xi_0) + \text{Ai}'(\xi_0)) \quad \text{and} \quad \kappa(\xi_0) = \int_{\xi_0}^{\infty} \text{Ai}(t) dt. \quad (4.20)$$

680 The above result with  $A_1 = 0$  was derived by Smith (1979a) for the flow through pipes  
 681 and for the more general case  $A_1 \neq 0$  by Hall & Smith (1990), Walton (1996) and Walton  
 682 & Patel (1998) as part of the vortex-wave interaction equations. Note that the lower-  
 683 branch viscous streak instability is controlled at leading order by the spanwise-dependent  
 684 wall shear  $\lambda_u$ , independent of the detailed wall-normal distribution of the streaky flow  
 685 velocity. For a general streaky base flow, the wall shear may be computed by other means  
 686 (e.g. by solving the N-S equations). This quantity can, after being rescaled according to  
 687 (2.11), be used in the stability equation (4.19). Alternatively, equation (4.19) may, again  
 688 by using (2.11), be recast to conform to the normalisation adopted in the calculation of  
 689 the streaky flow.

#### 690 4.5. Solving the eigenvalue problem for the viscous instability of the streaky flow

691 Since the coefficients of (4.19) are periodic functions of  $\hat{Z}$ , Floquet theory can be used  
 692 to express the pressure in both the upper and main decks, and the displacement function  
 693  $A_1$  in the form,

$$(P_1, p^\dagger, A_1) = \exp(iq\beta\hat{Z}) \sum_{n=-\infty}^{\infty} (\bar{P}_n, \bar{p}_n(y^\dagger), \bar{A}_n) \exp(in\beta\hat{Z}), \quad (4.21)$$

694 where  $q$  is the Floquet exponent.

695 Floquet systems arise in many applications, and the present one differs from those in  
 696 some well-known situations in several aspects. In standard Floquet systems with time-  
 697 periodic coefficients (e.g. Mathieu type of equations), the Floquet exponent is calculated  
 698 as an eigenvalue and usually takes complex values. In the present problem,  $q$  needs to

699 be chosen to accommodate the flow conditions on the spanwise length longer than the  
700 spacing, and  $q$  may turn out to be complex-valued if the roughness and end conditions  
701 on this long scale give rise to a preferred direction along the span. We consider only  
702 the case where such a preference does not appear, and  $q$  must be taken to be real so  
703 that the solution remains bounded in the spanwise direction. Moreover, the value  $q$  is  
704 pre-assigned. Such a geometric constraint is the same as that in the secondary instability  
705 of Görtler vortices, for which most calculations were performed for  $q = 0$  and  $q = 1/2$ ,  
706 corresponding to the so-called fundamental and subharmonic modes (Hall & Horseman  
707 1991; Li & Malik 1995). Subharmonic and fundamental resonances were also the primary  
708 interest of the secondary-instability analysis of saturated T–S waves (Herbert 1988),  
709 where the periodicity is in the streamwise direction. Here,  $q$  will be allowed to take  
710 all permissible real values so that the modes represent the continued development of  
711 oncoming T–S waves.

712 After substituting (4.21) into (4.12), the solution subject to  $\bar{p}_n \rightarrow 0$  as  $y^\dagger \rightarrow \infty$  and  
713  $\bar{p}_n(0) = \bar{P}_n$ , is found as

$$\bar{p}_n = \bar{P}_n e^{-(\alpha^2 + \beta^2(q+n)^2)^{1/2} y^\dagger}. \quad (4.22)$$

714

It follows from (4.11) and (4.9), and the matching condition  $v^\dagger \rightarrow i\alpha A_1$  as  $y^\dagger \rightarrow 0$  that

$$\left. \frac{\partial p^\dagger}{\partial y^\dagger} \right|_{y^\dagger=0} = -\alpha^2 A_1.$$

715 Use of (4.22) in this yields the relationship between the pressure and the displacement  
716 function:

$$\bar{A}_n = \frac{1}{\alpha^2} \left[ \alpha^2 + \beta^2(q+n)^2 \right]^{1/2} \bar{P}_n. \quad (4.23)$$

Now, substituting (4.21) with (4.23) into equation (4.19), and expressing the coefficients  
of equation (4.19) as,

$$\frac{\lambda_u \hat{z}}{\lambda_u} \mathcal{G}(\xi_0) = \sum_{l=-\infty}^{\infty} R_l e^{i\beta l \hat{z}}, \quad \frac{(i\alpha \lambda_u)^{5/3} \text{Ai}'(\xi_0)}{\kappa(\xi_0)} = \sum_{l=-\infty}^{\infty} Q_l e^{i\beta l \hat{z}}, \quad (4.24a, b)$$

717 we find, after equating the coefficients of respective Fourier components, that

$$\left[ \alpha^2 + \beta^2(q+n)^2 \right] \bar{P}_n = - \sum_{j=-\infty}^{\infty} a_{n,j} \bar{P}_j, \quad (4.25)$$

718 where

$$a_{n,j} = R_{n-j} i\beta(q+j) + Q_{n-j} \left[ \alpha^2 + \beta^2(q+j)^2 \right]^{1/2} / \alpha^2. \quad (4.26)$$

719 The system of equations, (4.25), is of infinite dimension, but if truncated, by restricting  
720  $-N \leq n \leq N$ , it can be expressed in the matrix form:

$$\mathbf{M} \bar{\mathbf{P}} = \mathbf{0}, \quad (4.27)$$

721 where

$$\bar{\mathbf{P}} = (\bar{P}_{-N}, \bar{P}_{-N+1}, \dots, \bar{P}_0, \dots, \bar{P}_N)^\top, \quad \mathbf{M} = \mathbf{I} \mathbf{M}_1(\alpha) + \mathbf{M}_2(\alpha, \omega, \lambda_u), \quad (4.28)$$

722 with  $\mathbf{I}$  being the identity matrix,  $\mathbf{M}_1$  being the vector

$$\mathbf{M}_1 = (\alpha^2 + \beta^2(q-N)^2, \alpha^2 + \beta^2(q-N+1)^2, \dots, \alpha^2 + \beta^2(q+N)^2)^\top, \quad (4.29)$$

723 and  $\mathbf{M}_2$  a full matrix with elements

$$(724) \quad (\mathbf{M}_2)_{n,j} = a_{n,j}. \quad (4.30)$$

724 Note that  $\bar{\mathbf{P}}$  contains  $2N + 1$  elements, the matrix  $\mathbf{M}$  is of size  $(2N + 1) \times (2N + 1)$ , and  
 725  $R_{n-j}$  and  $Q_{n-j}$  are both vectors of dimension  $4N + 1$ . Typically,  $N = 32$  was found to  
 726 be sufficient. The implicit dispersion relation is thus

$$\mathcal{D}(\alpha) \equiv \det(\mathbf{M}(\alpha, \omega, \lambda_u, q)) = 0. \quad (4.31)$$

727 In the limiting case where the roughness is absent,  $\lambda_u = 1$ , and it follows that  $R_l = 0 \forall l$ ,  
 728 and  $Q_l = 0 \forall l \neq 0$ , giving the dispersion relation,

$$\mathcal{D}_B(\alpha) \equiv \alpha^2(\alpha^2 + \beta^2(q + n)^2)^{1/2} + (i\alpha)^{5/3} \text{Ai}'(\xi_0)/\kappa(\xi_0) = 0, \quad (4.32)$$

729 for the lower-branch T-S instability with  $\beta(q + n)$  being the spanwise wavenumber of  
 730 oblique modes. For the spatial instability problem, the frequency  $\omega$  is taken to be real,  
 731 while the complex streamwise wavenumber  $\alpha$  is to be found as the roots to equations  
 732 (4.31) or (4.32). This is done by using Muller's method (Muller 1956) in §5.

733 Equation (4.21) indicates that  $q$  can be restricted to  $-\frac{1}{2} \leq q \leq \frac{1}{2}$ , since any integer in  
 734  $q$  can be absorbed into the Fourier series. For symmetric streaks under consideration,  $q$   
 735 can be further restricted to  $0 \leq q \leq \frac{1}{2}$ . To show this, we note that the solution to (4.19)  
 736 for  $q = -\tilde{q}$ , with  $\tilde{q} > 0$ , is

$$P_1(\hat{Z}) = e^{-i\tilde{q}\beta\hat{Z}} \sum_{n=-\infty}^{\infty} \tilde{P}_n e^{in\beta\hat{Z}}. \quad (4.33)$$

737 The problem for  $\tilde{P}_n$  in (4.25) is then

$$\left[ \alpha^2 + \beta^2(n - \tilde{q})^2 \right] \tilde{P}_n = - \sum_{j=-\infty}^{\infty} \left( R_{n-j} i\beta(j - \tilde{q}) + Q_{n-j} \left[ \alpha^2 + \beta^2(j - \tilde{q})^2 \right]^{1/2} / \alpha^2 \right) \tilde{P}_j. \quad (4.34)$$

738 Since  $\lambda_u$  is symmetric about the centerline, it follows from (4.24) that  $R_l = -R_{-l}$  and  
 739  $Q_l = Q_{-l}$ , so (4.34) can be written as

$$\left[ \alpha^2 + \beta^2(\tilde{q} + n)^2 \right] \tilde{P}_{-n} = - \sum_{j=-\infty}^{\infty} \left[ R_{n-j} i\beta(\tilde{q} + j) + Q_{n-j} (\alpha^2 + \beta^2(\tilde{q} + j)^2)^{1/2} / \alpha^2 \right] \tilde{P}_{-j}, \quad (4.35)$$

740 which is of the form of (4.27)–(4.30) with  $\tilde{q} > 0$  and the eigenvector  $\tilde{P}_n = \bar{P}_{-n}$ . Therefore,  
 741 a root,  $\alpha$ , for  $q < 0$  can be related to one for  $q > 0$ . Without loss of generality,  $q$   
 742 is restricted to  $0 \leq q \leq 1/2$ . The two special cases,  $q = 0$  and  $1/2$ , refer to fundamental  
 743 and subharmonic instability respectively.

## 744 5. Numerical results for the stability problem

### 745 5.1. T-S mode for the flat-plate case

746 For a given real disturbance frequency  $\omega$ , the complex wavenumber,  $\alpha = \alpha_r + i\alpha_i$ , is  
 747 calculated using Muller's iteration method with an initial guess of  $3 - i0.4$ , for example.  
 748 For the usual T-S mode,  $\alpha_r$  and the growth rate ( $-\alpha_i$ ), obtained from the dispersion  
 749 relation (4.32), is shown in figure 12 for several representative values of

$$\beta_{TS} \equiv \beta(n + q). \quad (5.1)$$

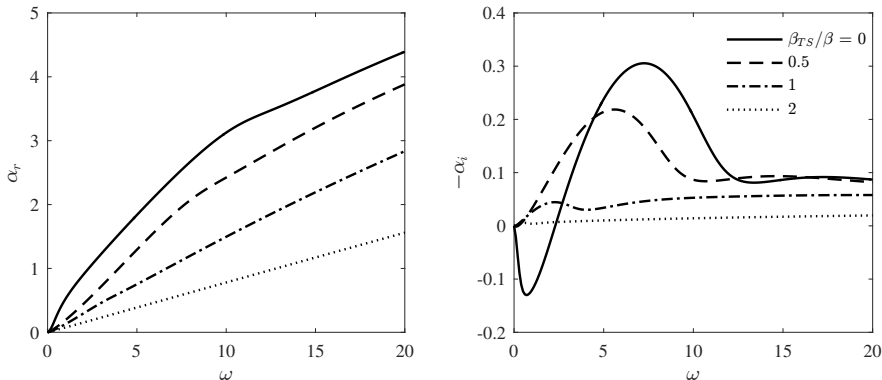


FIGURE 12. Instability characteristics of T-S modes with  $\beta_{TS}/\beta = n + q$ .

750 For most of the frequency regime, T-S modes with larger  $\beta_{TS}$  generally have smaller  
 751 growth rates, but in certain frequency ranges the growth rate,  $-\alpha_i$ , is not the largest for  
 752 the planar mode ( $\beta_{TS}/\beta = n + q = 0$ ).

### 5.2. Solutions in the presence of roughness elements

753  
 754 When roughness elements are present, the dispersion relation (4.31) is determined by  
 755 the spanwise dependent wall shear  $\lambda_u = \lambda_u(\hat{X}, \hat{Z}) = 1 + \tau_d(\hat{X}, 0, \hat{Z})$ . Far upstream of the  
 756 surface roughness, this value tends to unity and hence the dispersion relation is virtually  
 757 the same as that for the T-S modes.

758 Two properties of interest can be inferred from the Floquet analysis in §4.5. The first  
 759 is the multiplicity of the solutions. Each solution can be associated with, and thereby  
 760 distinguished by, its upstream behaviour, namely,

$$P_1(\hat{Z}) = e^{iq\beta\hat{Z}} \sum_{n=-\infty}^{\infty} \bar{P}_n e^{in\beta Z} \rightarrow \bar{P}_k e^{i(q+k)\beta\hat{Z}} \quad \text{as } \hat{X} \rightarrow -\infty, \quad (5.2)$$

761 where  $k$  is an integer and the right-hand side represents an oncoming T-S mode with  
 762 spanwise wavenumber  $\beta_{TS} = (q + k)\beta$  ( $k = 0, \pm 1, \pm 2, \dots$ ). The above association with  
 763 a single T-S mode is viable except when  $q = 1/2$  and  $q = 0$  but  $k \neq 0$ , as will be shown  
 764 below, where the exceptional cases will be discussed also.

765 With the Floquet exponent  $q$  being restricted to  $0 \leq q \leq 1/2$ , the notation for the  
 766 roots,  $\alpha$ , to (4.31) is as follows. Let  $\alpha_k(q)$  be a root to (4.31) at a given streamwise  
 767 location which can be traced upstream to the T-S mode with  $\beta_{TS}/\beta = q + k$ . Using this  
 768 notation, we can establish the following relations,

$$\alpha_k(q) = \alpha_{-k}(-q), \quad \alpha_k(q) = \alpha_{k+1}(q-1) \quad \left(0 < q < \frac{1}{2}\right). \quad (5.3)$$

769 The first expression above represents the equivalence of the growth rates of the modes  
 770 pertaining to  $\pm\beta_{TS}$ , while the second the multiplicity of solutions in (4.31).

771 Although the connection of an eigenmode to (4.31) with a pure T-S mode through (5.2)  
 772 is a parametric continuation, it actually represents the dynamic evolution of the latter  
 773 in the streamwise direction since non-parallelism is negligible to leading-order accuracy,  
 774 that is, despite being local in its nature, each mode in the streaky region describes the  
 775 continued development of an upstream T-S mode approaching the roughness (Piot *et al.*  
 776 2008). This connection with a single T-S mode upstream is one-to-one when  $q \neq 1/2$ ,

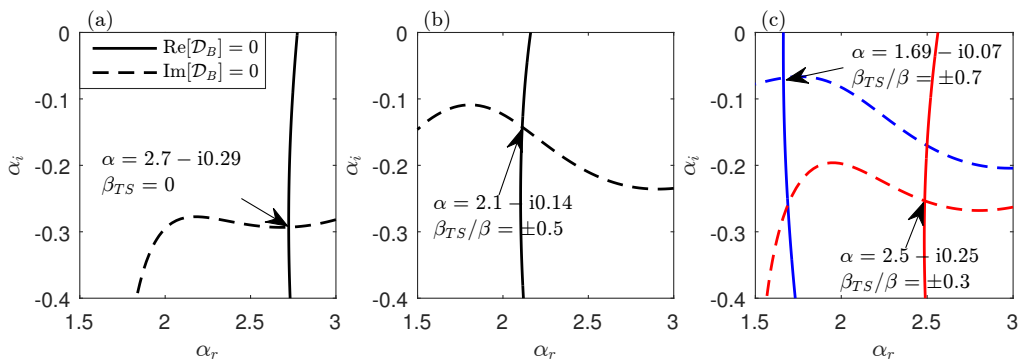


FIGURE 13. Contours of  $\mathcal{D}_{B,r} = 0$  and  $\mathcal{D}_{B,i} = 0$  for  $\beta_{TS}/\beta = 0, \pm 0.3, \pm 0.5$  and  $\pm 0.7$  for the flat-plate case and  $\omega = 8.2$ .

777  $q \neq 0$  as well as when  $q = 0$  and  $k = 0$ , but this is no longer true if  $q = 1/2$ , or  $q = 0$   
 778 but  $k \neq 0$ , in either case of which each mode in the streaky region is traced to a suitable  
 779 combination of two T-S modes with spanwise wavenumbers of equal size but of opposite  
 780 sign, as will be shown below. These cases can be viewed as the limits of  $q \uparrow 1/2$  and  $q \downarrow 0$ ,  
 781 leading to  $\alpha_k(q \uparrow \frac{1}{2})$  and  $\alpha_k(q \downarrow 0)$  ( $k \neq 0$ ) respectively.

782 The second point of interest is the symmetry of the eigensolution. If there exists a  
 783 symmetric eigensolution, i.e.  $P_1(\hat{Z}) = P_1(-\hat{Z})$ , then from (4.21) we have

$$e^{iq\beta\hat{Z}} \sum_{n=-\infty}^{\infty} \bar{P}_n e^{in\beta\hat{Z}} = e^{-iq\beta\hat{Z}} \sum_{n=-\infty}^{\infty} \bar{P}_n e^{-in\beta\hat{Z}}. \quad (5.4)$$

784 The above balance can be rewritten as

$$e^{iq\beta\hat{Z}} \sum_{n=-\infty}^{\infty} \bar{P}_n e^{in\beta\hat{Z}} = e^{i(K-q)\beta\hat{Z}} \sum_{n=-\infty}^{\infty} \bar{P}_{-(n+K)} e^{-in\beta\hat{Z}}, \quad (5.5)$$

785 which holds only if

$$q = K/2, \quad (5.6)$$

786 where  $K$  here is an integer (and should not be confused with  $k$ ). For a symmetric mode,  
 787 we have the relation

$$\bar{P}_n = \bar{P}_{-(n+K)}, \quad (5.7)$$

788 A similar argument shows that an antisymmetric mode,  $P_1(\hat{Z}) = -P_1(-\hat{Z})$ , is possible  
 789 if (5.6) holds, but now the relation

$$\bar{P}_n = -\bar{P}_{-(n+K)}. \quad (5.8)$$

790 The requirement (5.6) is a necessary condition for the existence of symmetric or anti-  
 791 symmetric modes. Numerical solutions show that such modes observing (5.7) or (5.8) do  
 792 exist. If  $q \neq K/2$ , the modes are neither symmetric nor antisymmetric.

793 Since  $q$  is restricted to the region  $0 \leq q \leq 1/2$ , there are only two choices,  $K = 0$  or  $1$ .  
 794 When  $q = 1/2$  ( $K = 1$ ), symmetric/anti-symmetric modes must necessarily consist of a  
 795 pair of oblique T-S modes,  $P_k e^{i(k+1/2)\beta\hat{Z}}$  and  $\pm P_{-(k+1)} e^{-i(k+1/2)\beta\hat{Z}}$  in the upstream limit  
 796 due to (5.7) or (5.8). Numerical solutions show that the symmetric and anti-symmetric  
 797 modes correspond to the limits of  $\alpha_{-(k+1)}(q \uparrow \frac{1}{2})$  and  $\alpha_k(q \uparrow \frac{1}{2})$ , which will for brevity

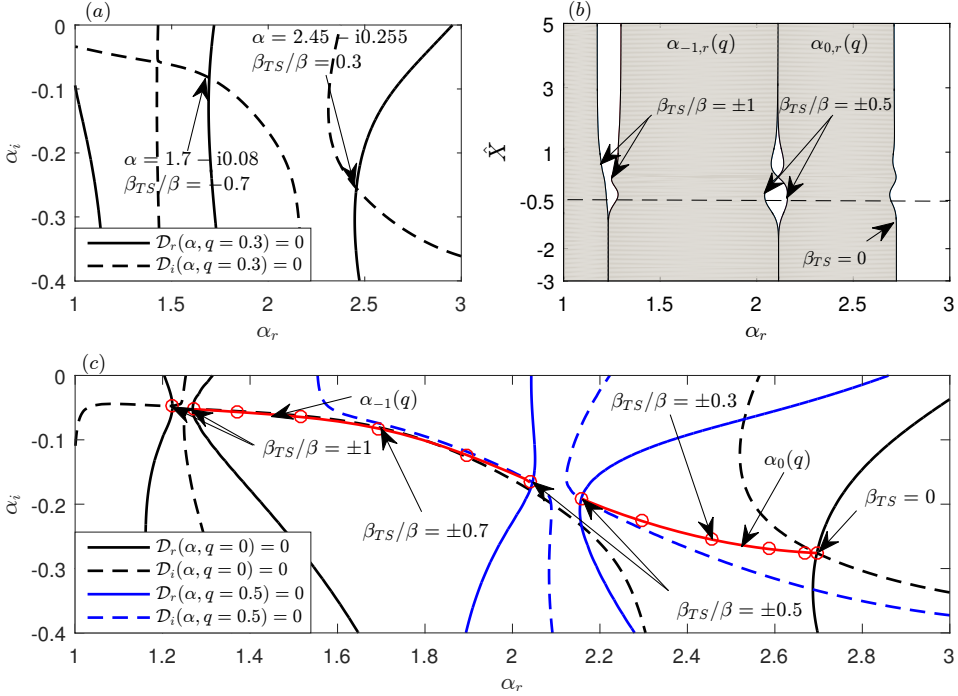


FIGURE 14. Dispersion properties at  $\hat{X} = -0.5$  for roughness shape 1 with  $\hat{h} = 0.15$  and frequency  $\omega = 8.2$ . (a) Contours of  $\mathcal{D}_r(\alpha)$  and  $\mathcal{D}_i(\alpha) = 0$  for  $q = 0.3$ . (b)  $\alpha_r$  versus  $\hat{X}$  for  $\beta_{TS}/\beta = 0, \pm 0.5$  and  $\pm 1$ . The curves border the shaded regions where a continuum of roots resides as  $\beta_{TS}$  is varied from 0 to  $\beta$ . The dashed line shows the streamwise location for the plots (a, c). (c) Eigenvalues of most unstable modes. The red line shows the continuum of the roots by varying  $q$  from 0 to 0.5 with an increment of 0.1. There are additional markers for the roots pertaining to symmetric and antisymmetric modes for  $\beta_{TS}/\beta = \pm 0.5$  and  $\pm 1$ .

798 be denoted as  $\alpha_{-(k+1)}(\frac{1}{2})$  and  $\alpha_k(\frac{1}{2})$  ( $k \geq 0$ ), respectively. Similarly, for  $q = 0$  ( $K = 0$ )  
 799 and  $k \neq 0$ , symmetric/anti-symmetric modes must consist of the two oblique T-S modes,  
 800  $P_k e^{ik\beta\hat{Z}}$  and  $\pm P_{-k} e^{-ik\beta\hat{Z}}$ , in the upstream limit due to (5.7) or (5.8). The symmetric  
 801 and anti-symmetric modes turn out to be the limits of  $\alpha_{-k}(q \downarrow 0)$  and  $\alpha_k(q \downarrow 0)$ , which  
 802 will for brevity be denoted as  $\alpha_{-k}(0)$  and  $\alpha_k(0)$  ( $k > 0$ ), respectively.

803 The roots of  $\mathcal{D}(\alpha) = 0$  correspond to the intersections of the two manifolds,  
 804  $\mathcal{D}_r(\alpha_r, \alpha_i) = 0$  and  $\mathcal{D}_i(\alpha_r, \alpha_i) = 0$ , where  $\mathcal{D}_r$  and  $\mathcal{D}_i$  denote the real and imaginary parts  
 805 of  $\mathcal{D}$  respectively. In order to locate the roots unmistakably, we map out  $\mathcal{D}_r(\alpha_r, \alpha_i) = 0$   
 806 and  $\mathcal{D}_i(\alpha_r, \alpha_i) = 0$  separately. Far upstream of the roughness elements, the roots to  
 807  $\mathcal{D}(\alpha) = 0$  for a given  $q$  essentially coincide with the roots to  $\mathcal{D}_B(\alpha) = 0$  for  $\beta_{TS}/\beta = q + k$ .  
 808 The latter are shown in figure 13 for  $\beta_{TS}/\beta = 0, \pm 0.3, \pm 0.5$  and  $\pm 0.7$  with  $\omega = 8.2$ .

809 The dispersion relation (4.31) was solved using Muller's method starting from a far  
 810 upstream location. The respective solutions from the flat-wall limit were used as the first  
 811 guess to/from which small complex numbers are added/subtracted, so that we have two  
 812 additional initial guesses necessary for the algorithm. The dispersion relation is solved  
 813 at the next location using the streamwise wavenumber from the previous streamwise  
 814 location as an initial guess.

815 As  $q$  is varied from 0 to  $1/2$ , the corresponding roots trace out the curves, which are



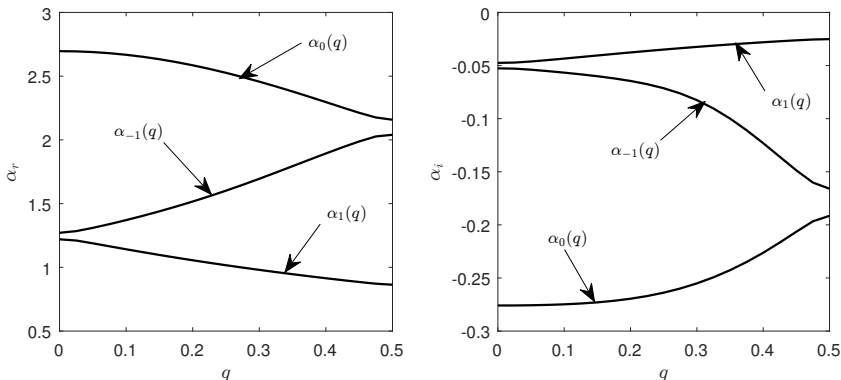


FIGURE 15. Real and imaginary parts of the roots  $\alpha_{0,-1,1}(q)$  at  $\hat{X} = -0.5$  for roughness shape 1,  $\hat{h} = 0.15$  and  $\omega = 8.2$ .

816 shown by the red lines with symbols in figure 14(c), corresponding to  $\alpha_0(q)$  and  $\alpha_{-1}(q)$ .  
 817 Hence a continuum of modes at a fixed location can be traced back to upstream T–S  
 818 modes with different spanwise wavenumbers. Each eigenvalue is of course an intersection  
 819 of  $\mathcal{D}_r = 0$  and  $\mathcal{D}_i = 0$ . This is shown for  $q = 0.3$  and  $0.7$  in figure 14(a). The curves and  
 820 their intersections in this figure can be viewed as arising from the continuous deformations  
 821 of those in figure 13(c). The right and left intersection points can be designated as modes  
 822  $\alpha_0(0.3)$  and  $\alpha_{-1}(0.3)$  respectively.

823 The intersections and roots for  $q = 0$  are displayed in figure 14(c), and they represent  
 824 modes  $\alpha_0(0)$ ,  $\alpha_{-1}(0)$  and  $\alpha_1(0)$ , the first of which represents the development of an  
 825 upstream planar T–S mode (figure 13a), whilst the latter two develop from upstream  
 826 oblique T–S modes with  $\beta_{TS} = \beta$  and  $-\beta$ , which have the identical growth rate and  
 827 streamwise wavenumber as is shown in figure 14(b). However, these modes can be  
 828 distinguished even in the upstream limit by their symmetry:  $\alpha_1(0)$  is antisymmetric and  
 829  $\alpha_{-1}(0)$  is symmetric. How oblique T–S modes with spanwise wavenumbers  $\pm\beta$  would  
 830 develop depends on the symmetry. If the spanwise velocities of the T–S modes have the  
 831 same magnitude and sign (sinuous configuration), they will evolve into the pure  $\alpha_1(0)$   
 832 mode; if the spanwise velocities are equal in amplitude but of opposite sign (varicose  
 833 configuration), the T–S modes will evolve into the pure  $\alpha_{-1}(0)$  mode. For the general  
 834 case where the spanwise velocities for  $\pm\beta$  T–S modes have different magnitudes, both  
 835 modes  $\alpha_1(0)$  and  $\alpha_{-1}(0)$  would emerge, and the perturbation is a linear combination of  
 836 the two.

837 Also shown in figure 14(c) are intersections for  $q = 1/2$  and the resulting roots,  
 838 which can be designated as  $\alpha_0(1/2)$  and  $\alpha_{-1}(1/2)$ . Similarly to the case of  $q = 0$ ,  
 839 they merge in the upstream limit now with the T–S modes with  $\beta_{TS} = \pm\beta/2$  (figure  
 840 14b), but may be distinguished by their symmetry properties ( $\alpha_0(1/2)$  antisymmetric,  
 841  $\alpha_{-1}(1/2)$  symmetric). The development of the T–S modes with spanwise wavenumbers  
 842  $\pm\beta/2$  depends on their symmetry.

843 Figure 15 displays the real and imaginary parts of three modes of main interest:  $\alpha_0(q)$ ,  
 844  $\alpha_1(q)$ , and  $\alpha_{-1}(q)$  for  $0 \leq q \leq 1/2$ . The two modes for  $q = \frac{1}{2}$  in figure 14(c) should be  
 845 viewed as the limiting values as  $q \uparrow \frac{1}{2}$ :  $\alpha_0(q \uparrow \frac{1}{2})$  and  $\alpha_{-1}(q \uparrow \frac{1}{2})$ . These roots pertain  
 846 to antisymmetric and symmetric modes, respectively, shown in figure 16. The differences  
 847 between the real parts of  $\alpha_0(q \uparrow \frac{1}{2})$  and  $\alpha_{-1}(q \uparrow \frac{1}{2})$ , and  $\alpha_{-1}(q \downarrow 0)$  and  $\alpha_1(q \downarrow 0)$  along  
 848 the streamwise direction can be seen in figure 14(b). The modes  $\alpha_0(\hat{X}, q)$ ,  $\alpha_{-1}(\hat{X}, q)$  and  
 849  $\alpha_1(\hat{X}, q)$  for  $0 < q < 1/2$  distribute continuously in the shaded regions from the right to

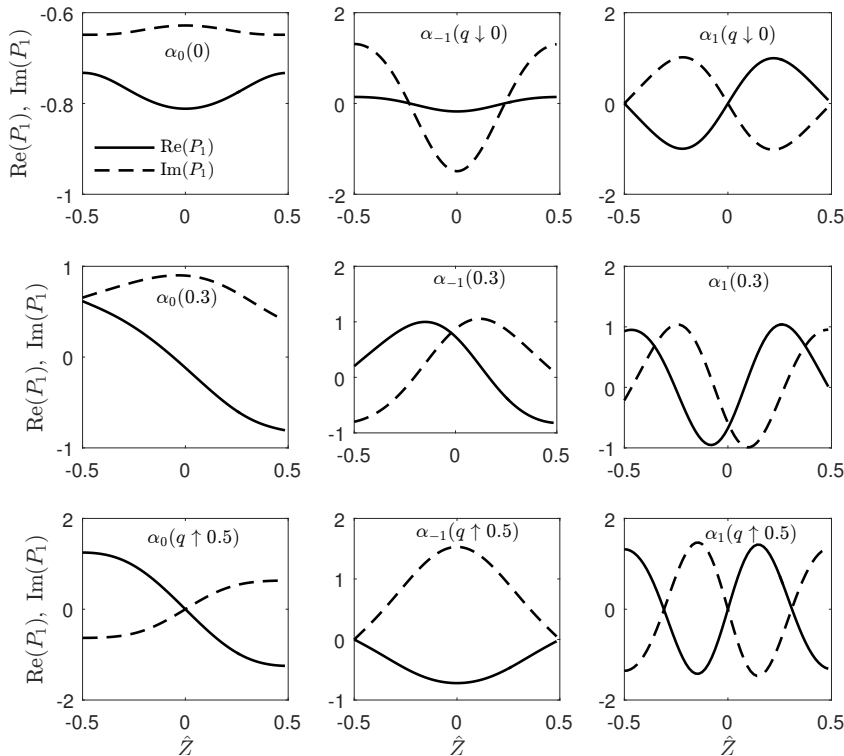


FIGURE 16. Shapes of  $P_1(\hat{Z})$  of the mode  $\omega = 8.2$  at  $\hat{X} = -0.5$  in the case of roughness shape 1 with  $\hat{h} = 0.15$ .

850 the left, respectively. While the blank regions signify the discontinuity of the roots when  
 851  $q = \pm 1/2, \pm 1$ .

852 The shapes of  $P_1(\hat{Z})$  for a few representative modes are displayed in figure 16. Figures  
 853 15 and 16 show that the antisymmetric mode has a larger growth rate compared to  
 854 the symmetric mode as  $q \uparrow \frac{1}{2}$ . However, the opposite is true as  $q \downarrow 0$ , since  $\text{Im}[\alpha_0(q \downarrow 0)] < \text{Im}[\alpha_{-1}(q \downarrow 0)] < \text{Im}[\alpha_1(q \downarrow 0)]$ . For  $q \neq \frac{1}{2}K$ , the mode exhibits no symmetry  
 855 at all. The multiplicity and symmetric properties revealed here are fairly generic for  
 856 a parametric instability governed by differential equations with periodic coefficients.  
 857 These are some simple but new results, which do not appear to have been recognised or  
 858 presented thoroughly before.  
 859

860 In the following sections, we only consider the modes  $0 \leq \beta_{TS}/\beta \neq \frac{1}{2}$  as the growth  
 861 rates are the same for  $\pm\beta_{TS}$ . For the special case,  $\beta_{TS}/\beta = \frac{1}{2}$ , we consider the mode  
 862 with the larger growth rate.

863 The local growth rates obtained for the three different roughness shapes are shown  
 864 in figures 17, 18 and 19. In the vicinity of the roughness, the most unstable plane T-S  
 865 wave ( $\beta_{TS} = 0$ ) is attenuated appreciably for  $\omega = 5$  and 8.2, but not for  $\omega = 10$ , where  
 866 destabilisation is observed. Appreciable growth rate reduction occurs, however, in the  
 867 wake for frequencies  $\omega = 5$  and 8.2. For  $\beta_{TS}/\beta = 0.25$ , a similar behaviour is observed  
 868 compared to the  $\beta_{TS} = 0$  case with the difference being that the stabilisation effect on  
 869 the mode with  $\omega = 8.2$  is very moderate. When the plots of the left and the central  
 870 columns ( $\beta_{TS}/\beta = 0.25$ ) of figure 18 are compared with the respective ones of figure 17,

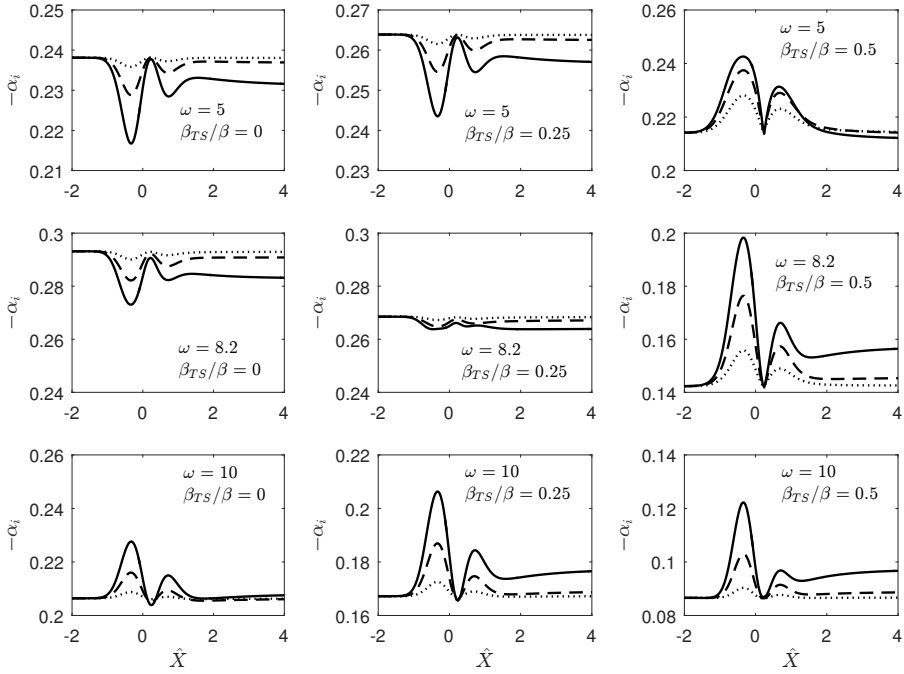


FIGURE 17. The local growth rate ( $-\alpha_i$ ) versus  $\hat{X}$  for roughness shape 1. Solid lines:  $\hat{h} = 0.15$ ; dashed lines:  $\hat{h} = 0.1$ ; dotted lines:  $\hat{h} = 0.05$ . Left column:  $\beta_{TS} = 0$ ; center column:  $\beta_{TS}/\beta = 0.25$ ; right column:  $\beta_{TS}/\beta = 0.5$ .

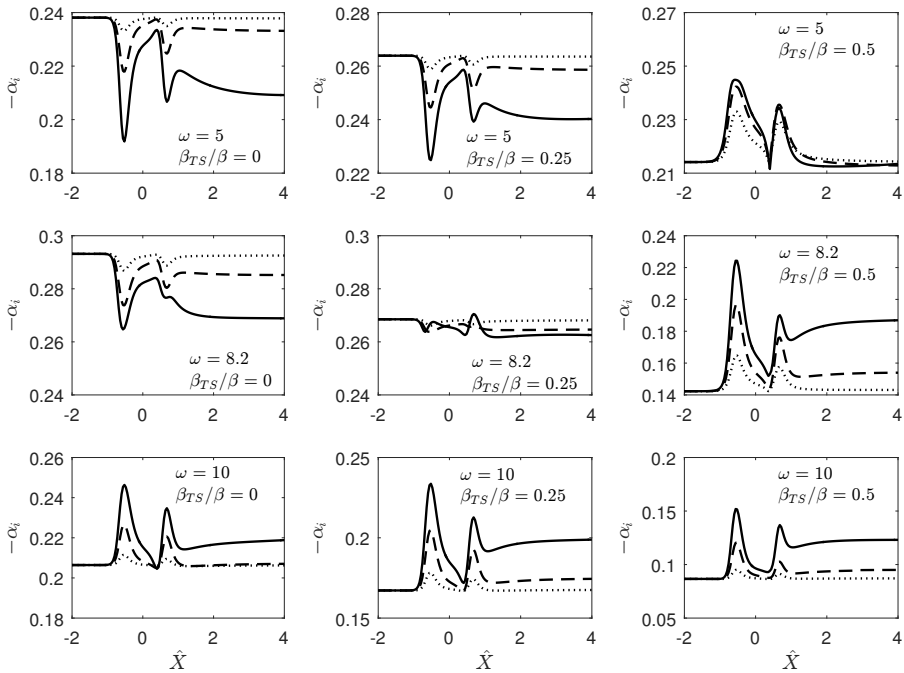


FIGURE 18. The local growth rate ( $-\alpha_i$ ) versus  $\hat{X}$  for roughness shape 2. Solid lines:  $\hat{h} = 0.15$ ; dashed lines:  $\hat{h} = 0.1$ ; dotted lines:  $\hat{h} = 0.05$ . Left column:  $\beta_{TS} = 0$ ; center column:  $\beta_{TS}/\beta = 0.25$ ; right column:  $\beta_{TS}/\beta = 0.5$ .

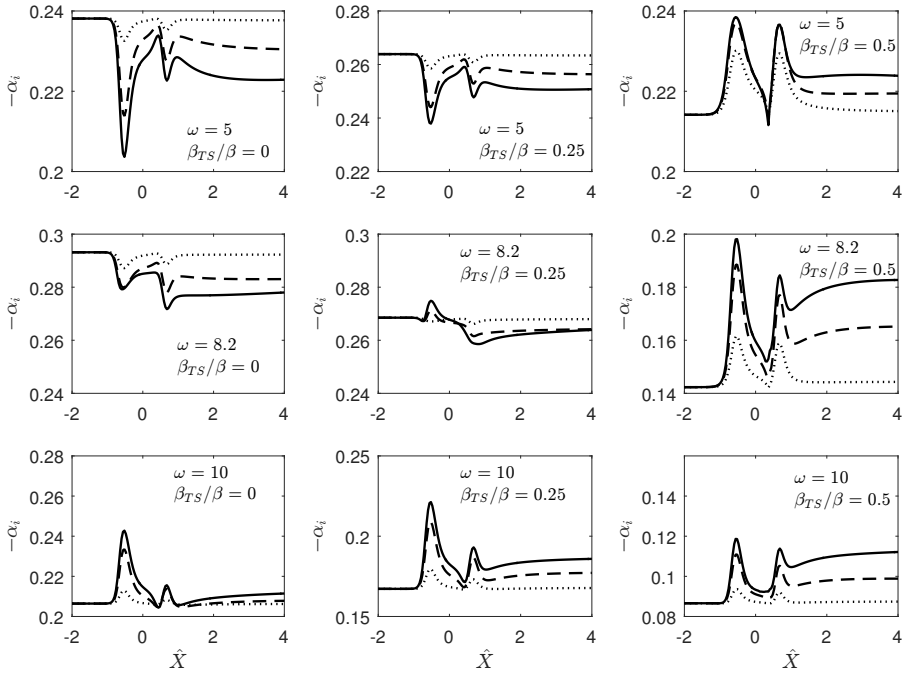


FIGURE 19. The local growth rate ( $-\alpha_i$ ) versus  $\hat{X}$  for roughness shape 3. Solid lines:  $\hat{h} = 0.12$ ; dashed lines:  $\hat{h} = 0.1$ ; dotted lines:  $\hat{h} = 0.05$ . Left column:  $\beta_{TS} = 0$ ; center column:  $\beta_{TS}/\beta = 0.25$ ; right column:  $\beta_{TS}/\beta = 0.5$ .

871 one notices that for  $\hat{h} = 0.15$ , the stabilisation is stronger in the case of roughness shape  
 872 2, implying that the step streamwise shape is more advantageous for these modes.

873 The results are different for highly oblique waves ( $\beta_{TS}/\beta = 0.5$ ), as is indicated by the  
 874 plots in the right columns of figures 17-19. Destabilisation is observed for all frequencies  
 875 over the roughness elements, and it is significant even for a very small roughness height,  
 876  $\hat{h} = 0.05$ . The strong destabilisation is expected because of the subharmonic parametric  
 877 resonance. The results in figures 17-19 also support the observation made by Downs &  
 878 Fransson (2014) that streaks of higher amplitude (but still without exceeding a critical  
 879 height) are more stabilising.

880 The results in figures 18 and 19 appear similar because they are for roughness elements  
 881 which share the same streamwise shape, whereas the results in figure 17, which are for  
 882 roughness shape 1, exhibit less similarity to those in figures 18 and 19. The contrast  
 883 suggests that the streamwise shape of the roughness elements has a greater effect on the  
 884 growth rate than the spanwise shape.

885 Interestingly, most of the growth rate curves in figures 17-19 exhibit two dips (or  
 886 humps). This may seem unexpected considering the single peaked roughness shape.  
 887 However, we have to keep in mind that the quantity determining the growth rate is  
 888  $\lambda_u$ , certain features of which as shown in figure 4 may therefore underpin the general  
 889 shape of the growth rate curves: for example  $\lambda_u$  along the centerline ( $\hat{Z} = 0$ ) has two  
 890 local minima rather than featuring a single peak (or valley).

891 The overall effect of the roughness can be measured by the change of the N-factor,

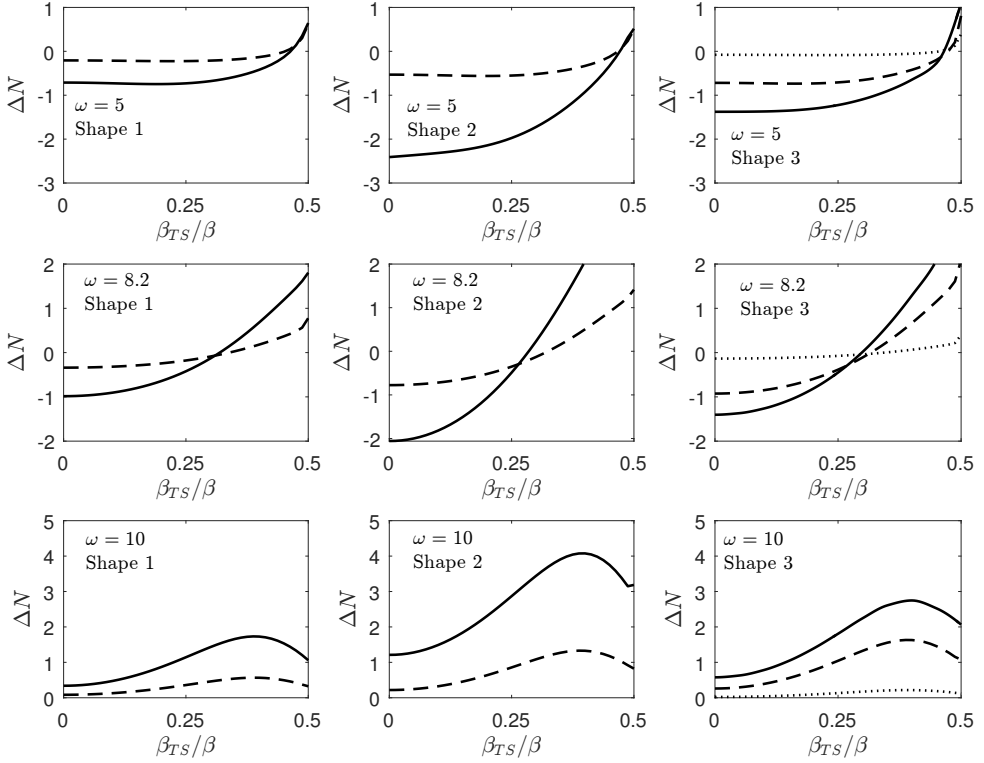


FIGURE 20.  $\Delta N$ -factor for various roughness shapes and frequencies. Left column: roughness shape 1. Central column: roughness shape 2. Right column: roughness shape 3. In the first and second columns: dashed is  $\hat{h} = 0.1$  and solid is  $\hat{h} = 0.15$ . Right column: solid is  $\hat{h} = 0.12$ , dashed is  $\hat{h} = 0.1$  and dotted is  $\hat{h} = 0.05$ .

892 which is defined by

$$\Delta N(\omega, \beta_{TS}) = \epsilon_1^{-1} \int_{-\infty}^{\hat{X}=5} [(-\alpha_i) - (-\alpha_i)_0] d\hat{X}, \quad (5.9)$$

893 where  $(-\alpha_i)_0$  is the growth rate in the flat-plate case for given  $(\omega, \beta_{TS})$ . Note that the  
 894 upper limit  $\hat{X} = 5$  already includes the extended wake region extending more than  
 895 4 times the distance between the roughness centre and leading edge, and covers the  
 896 majority of the amplification phase. The overall stabilization effect is unlikely to be  
 897 altered qualitatively by the wake farther downstream, but the quantitative influence of  
 898 the latter requires further investigations. The columns in figure 20 pertain to the three  
 899 different wall shapes, while each row to a different frequency. For  $\omega = 5$ , stabilisation  
 900 is observed for weakly oblique modes with spanwise wavenumbers between 0 and  $0.4\beta$ .  
 901 However, for larger  $\beta_{TS}$  the stabilising effect of the streaks diminishes. In particular,  
 902 for  $\beta_{TS}/\beta = 0.5$  the streaks play a destabilising role for all three wall shapes due to  
 903 the subharmonic parametric resonance. In general, a similar behaviour is observed for  
 904  $\omega = 8.2$  with the difference that destabilisation occurs for lower  $\beta_{TS}$  values. For  $\omega = 10$ ,  
 905 destabilisation occurs for all values of  $\beta_{TS}$ . In general, plane T-S waves ( $\beta_{TS} = 0$ ) are  
 906 found to be stabilised the most for each wall shape and frequencies  $\omega = 5$  and  $8.2$ , while  
 907 strongly oblique modes tend to be destabilised. Figure 20 also shows that increasing  
 908 the roughness height enhances the stabilising or destabilising effect as it is observed for

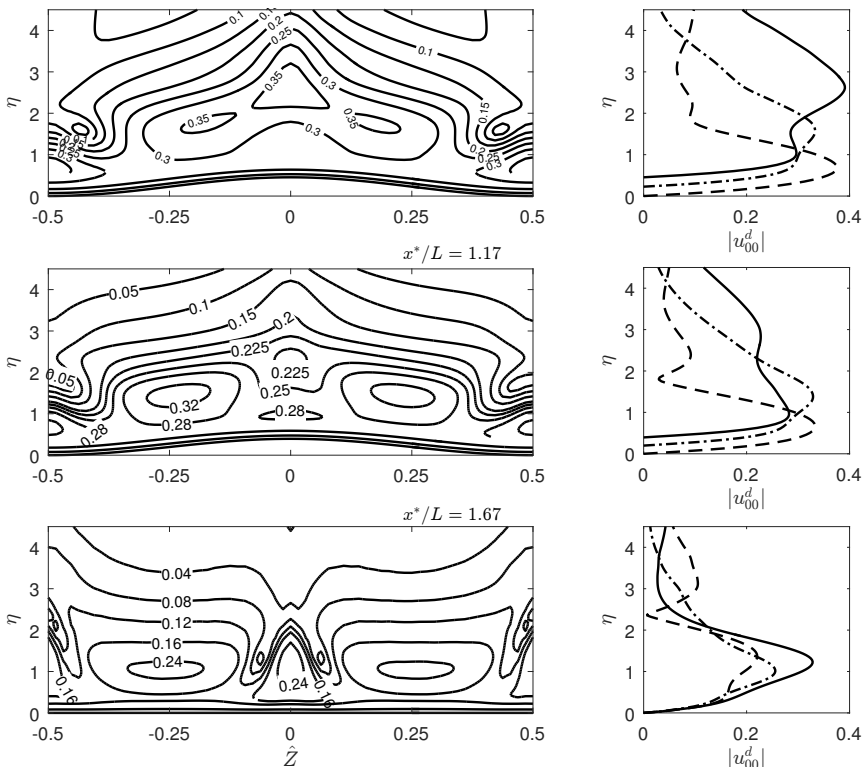


FIGURE 21. Left column: contours in  $y$ - $z$  plane of the eigenfunction  $|u_{00}^d|$  ( $\beta_{TS} = 0$ ). Right column: profiles of  $|u_{00}^d|$  at  $\hat{Z}/\Lambda = 0$  (solid line), 0.25 (dot-dashed line), 0.5 (dashed line). The parameter values are  $\omega = 8.2$  and  $\hat{h} = 0.15$ . Roughness shape 2.

909 example by Siconolfi *et al.* (2015). The result suggests that roughness shape matters  
 910 considerably to the effectiveness of inhibiting the instability with shape 3 being the best  
 911 of all three for a given roughness height.

912 The composite solution for the streamwise velocity of the eigenfunction can be con-  
 913 structed using the disturbance solutions in the main- and lower decks. For this purpose,  
 914 the eigenvector of (4.27) is calculated using the built-in function in MATLAB. Then the  
 915 expressions for  $P_1$ , and its first and second derivatives with respect to  $\hat{Z}$  are obtained  
 916 using (4.21). The leading-order lower- and main-deck streamwise velocities match since  
 917 both tend to  $\lambda_u A_1$  as  $Y^\dagger \rightarrow \infty$  and  $\check{y} \rightarrow 0$ , respectively. Because the leading-order main-  
 918 deck velocity tends to zero as  $\check{y} \rightarrow \infty$ , for a qualitative demonstration of the disturbance  
 919 eigenfunction in the main- and lower-deck regions, it suffices to construct the first-order  
 920 composite solution, namely,

$$u_{00}^d = \lambda_B^{1/4} (U_1 + u_1 - \lambda_u A_1), \quad (5.10)$$

921 where  $U_1$  is given by equation (A 1) in Appendix A, and  $u_1$  is the main-deck solution,  
 922 given by (4.9a) with  $u_b$  in this case being the Blasius profile that has been altered due  
 923 to the roughness elements.

924 Figure 21 shows the distribution of the eigenfunction,  $|u_{00}^d|$ , including the contours in  
 925 the  $y$ - $z$  plane and the typical wall-normal profiles at various streamwise locations for  
 926 roughness shape 2. Some similarities can be observed between the present theoretical  
 927 results (shown in the last two rows in the figure) and the experimental measurements of

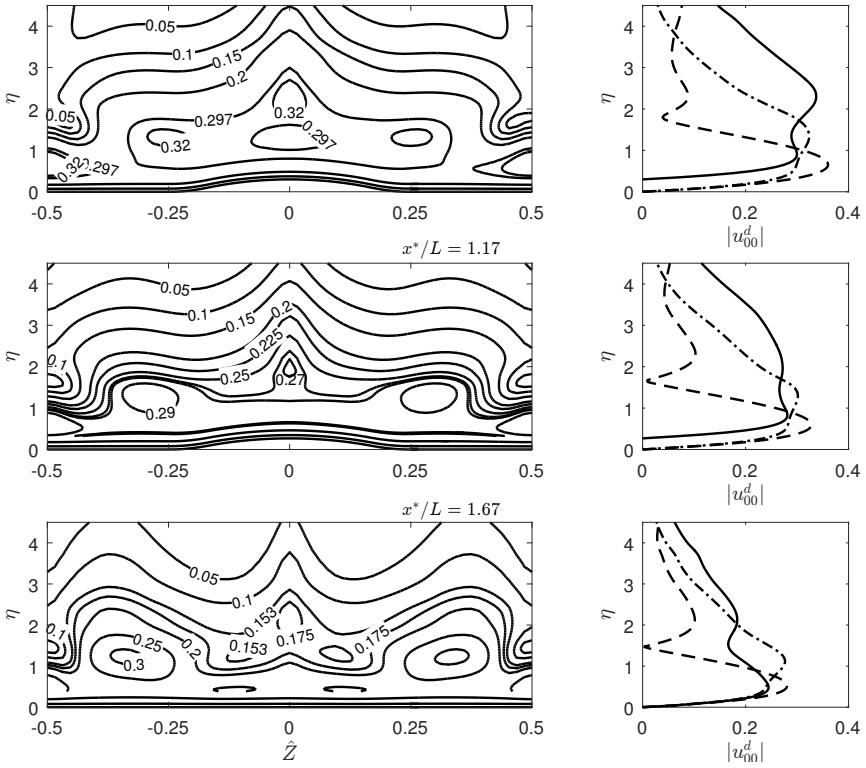


FIGURE 22. Left column: contours in  $y$ - $z$  plane of the eigenfunction  $|u_{00}^d|$  ( $\beta_{TS} = 0$ ). Right column: profiles of  $|u_{00}^d|$  at  $\hat{z}/\Lambda = 0$  (solid line), 0.25 (dot-dashed line), 0.5 (dashed line). The parameter values are  $\omega = 8.2$  and  $\hat{h} = 0.1$ . Roughness shape 3.

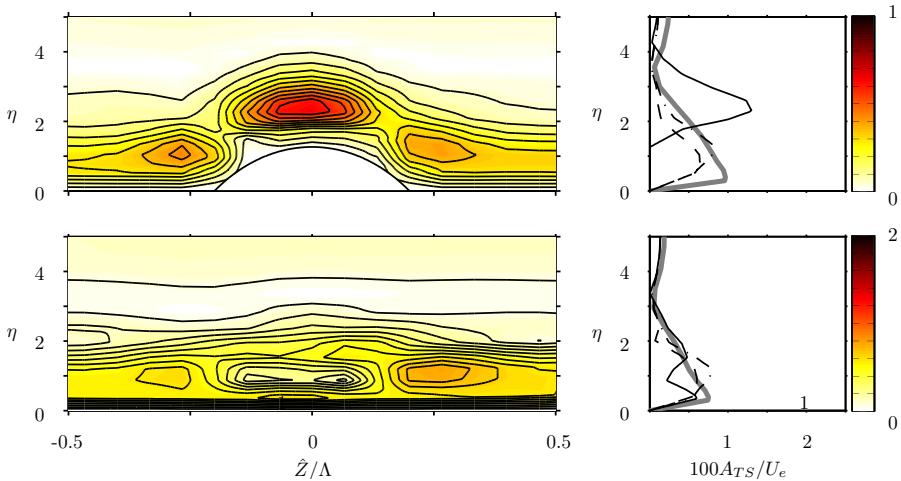


FIGURE 23. Experimental results from Downs & Fransson (2014): contours of the T-S-wave amplitude,  $A_{TS}$ , where  $U_e$  is the slip velocity. The reader is referred to Downs & Fransson (2014) for the definitions of these quantities. The top and bottom rows correspond to  $x^*/L = 1.17$  and 1.67, respectively. The amplitude profiles at  $\hat{z}/\Lambda = 0$ , 0.25 and 0.5 are plotted as solid, dot-dashed, and dashed lines, respectively. The frequency is set to  $\omega = 8.2$ .

Downs & Fransson (2014), which are reproduced in figure 23. The similarities include the three local maxima about the centerline ( $\hat{Z}/\Lambda = 0$ ) and near  $\hat{Z}/\Lambda = \pm 0.25$ , and the M-shape of the amplitude profiles at  $x^*/L = 1.17$ . Similar features at  $x^*/L = 1.67$  can also be noted for the eigenfunction contours, where a pair of maxima near  $\hat{Z}/\Lambda = \pm 0.25$  can be seen in both the theoretical and experimental results. In addition, a pair of minima are present near  $\hat{Z}/\Lambda = \pm 0.075$  next to the central maximum.

Figure 22 also displays the distribution of the eigenfunction,  $|u_{00}^d|$ , but now for roughness shape 3. The bottom two contour plots in this figure mimic the experimental results of Downs & Fransson (2014) in figure 23 very well. At  $x^*/L = 1.17$ , in addition to the central maximum, a pair of maxima near  $\hat{Z}/\Lambda = \pm 0.28$  are present in the respective contours in figures 22 and 23, respectively. Further downstream, at  $x^*/L = 1.67$ , two maxima near  $\hat{Z}/\Lambda = \pm 0.3$  and two minima at  $\hat{Z}/\Lambda = \pm 0.15$  can be observed. The profile of  $|u_{00}^d|$  at the centerline contains a peak close to the wall and a second peak at  $\eta \approx 2$ , giving rise to an ‘M’-shaped distribution, while the profile at  $\hat{Z}/\Lambda = 0.25$  has a single peak at  $\eta \approx 1$ . The measured profiles shown in figure 23 clearly exhibit these features.

## 6. Conclusions

Motivated by recent experimental observations, we carried out a theoretical study of the possible stabilising effect of spanwise periodic roughness elements on the lower-branch T–S instability. The spanwise length scale was taken to be comparable with the characteristic wavelength of T–S modes, while the streamwise length scale is much longer.

The present analysis was based on a high-Reynolds-number asymptotic approach. The equations governing the roughness-induced steady flow were obtained through the introduction of a stretched streamwise variable of the standard triple-deck formulation for fully three-dimensional humps studied by Duck & Burggraf (1986). In doing so, the roughness height was taken to be such that the wall shear was altered by an  $O(1)$  amount and became spanwise dependent. This led to a fully nonlinear system, which is elliptic in the spanwise direction but parabolic in the streamwise direction. The parabolic system provides an effective means for assessing the impact of roughness as it can be solved efficiently by a streamwise marching method. Numerical solutions showed that downstream of each roughness element there emerged a streaky structure consisting of four alternating low- and high-speed regions within one period in the spanwise direction.

The linear stability of the streaky flow was analysed. The instability is viscous and bi-global in its nature (Piot *et al.* 2008; Theofilis 2011). In the high-Reynolds-number limit, it remains governed by the classical triple-deck structure as in the absence of the roughness (Smith 1979*b*). By taking advantage of the asymptotic structure the instability is shown to be controlled by the spanwise dependent wall shear. The stability problem is reduced to an ordinary differential equation, which is the same as that in Hall & Smith (1990) and Walton (1996). The reduction of a viscous bi-global instability problem to a one-dimensional eigenvalue problem in the spanwise direction reduces substantially the computational cost, but also provides insight into the mechanism of the stabilisation. As the coefficients of the governing equation are periodic functions of the spanwise variable, the problem was solved using Floquet theory, giving rise to a system of linear equations of infinite dimension. The appropriately truncated system was solved numerically using Muller’s iterative method to obtain the local spatial growth rates for various disturbance frequencies and spanwise wavenumbers. The parametric study found that plane and weakly three-dimensional T–S waves with moderate frequencies were generally stabilised while modes with sufficiently high frequencies were destabilised over the roughness elements and in the wake downstream. In particular, strong destabilisation was observed



for waves with half the wavenumber of the periodic roughness array. The result suggests that the destabilisation effect can be prevented by creating streaks of small spacing.

A preliminary comparison showed a good qualitative agreement between the present theoretical predictions and the experimental data of Downs & Fransson (2014) and Fransson *et al.* (2004). The topological structure of the eigenfunctions resembles those measured in the experiments.

Our calculations suggested that roughness shapes have an intriguing impact on the character of the streaky flow and in turn on its linear stability. Hence further work could seek to optimise the shape of the roughness so that the greatest stabilisation of the instability is achieved. Another extension would be to investigate the long-range persistence of the wakes behind the roughness elements. An analysis similar to that of Goldstein *et al.* (2010, 2016) may be conducted to characterize the far wake and quantify its stabilising effect. This would allow for comparisons with experimental data to be made in a larger streamwise region, which many experiments have already covered. Naturally, for the precise quantification of the accuracy of the asymptotic theory as applied at moderate Reynolds numbers for both the streaky base flow and its instability, it is necessary to resort to solving the full N-S equations; this is another topic to be investigated in the future.

The authors would like to thank Professors A. I. Ruban and J. H. M. Fransson for helpful discussions. This research was supported by the EPSRC-funded Centre for Doctoral Training in Fluid Dynamics across Scales (grant EP/L016230/1), and was part of the LFC-UK project (grant EP/I1037946/1). The referees are thanked for their comments which helped improve the paper.

## Declaration of Interests

The authors report no conflict of interest.

## Appendix A. Stability calculations

The solution to equation (4.16) can be shown to be:

$$U_1 = B_1 \int_{\xi_0}^{\xi} \text{Ai}(t) dt + \left( \psi_1 - \frac{3}{4} \phi_1 \right) \text{Ai}(\xi) + \left( \psi_2 - \frac{3}{4} \phi_2 \right) \text{Gi}(\xi) + \frac{\phi_1}{4} \xi \text{Ai}'(\xi) + \frac{\phi_2}{4} \xi \text{Gi}'(\xi) - \left( \psi_1 - \frac{3}{4} \phi_1 \right) \text{Ai}(\xi_0) - \left( \psi_2 - \frac{3}{4} \phi_2 \right) \text{Gi}(\xi_0) - \frac{\phi_1}{4} \xi_0 \text{Ai}'(\xi_0) - \frac{\phi_2}{4} \xi_0 \text{Gi}'(\xi_0), \quad (\text{A } 1)$$

where

$$B_1 = \frac{i\alpha P_1}{\text{Ai}'(\xi_0)(i\alpha\lambda_u)^{2/3}} - \left[ \frac{\phi_1 \xi_0^2}{4} + \frac{1}{\text{Ai}'(\xi_0)} \left( \xi_0 \psi_1 \text{Ai}(\xi_0) + \xi_0 \psi_2 \text{Gi}(\xi_0) + \frac{\phi_2 \xi_0^2}{4} \text{Gi}'(\xi_0) + \frac{\phi_2 - 4\psi_2}{4\pi} \right) \right], \quad (\text{A } 2)$$

$$\psi_1 = \frac{\pi \lambda_u \hat{z} P_{1\hat{z}}}{(i\alpha\lambda_u)^{5/3}} \left[ \frac{5\text{Gi}(\xi_0)}{3\text{Ai}(\xi_0)} + \frac{2}{3} \xi_0 \left( \frac{\text{Gi}'(\xi_0)}{\text{Ai}(\xi_0)} - \frac{\text{Gi}(\xi_0)\text{Ai}'(\xi_0)}{\text{Ai}^2(\xi_0)} \right) \right] - \frac{\text{Gi}(\xi_0)}{\text{Ai}(\xi_0)} \frac{\lambda_u \pi P_{1\hat{z}\hat{z}}}{(i\alpha\lambda_u)^{5/3}},$$

$$\psi_2 = \frac{\lambda_u \pi P_{1\hat{z}\hat{z}}}{(i\alpha\lambda_u)^{5/3}} - \frac{5\pi \lambda_u \hat{z} P_{1\hat{z}}}{3(i\alpha\lambda_u)^{5/3}}, \quad \phi_1 = \frac{2}{3} \frac{\text{Gi}(\xi_0)}{\text{Ai}(\xi_0)} \frac{\pi \lambda_u \hat{z} P_{1\hat{z}}}{(i\alpha\lambda_u)^{5/3}}, \quad \phi_2 = -\frac{2}{3} \frac{\pi \lambda_u \hat{z} P_{1\hat{z}}}{(i\alpha\lambda_u)^{5/3}}.$$

## REFERENCES

- 1005 ABRAMOWITZ, M. & STEGUN, I. A. 1964 *Handbook of Mathematical Functions with Formulas,*  
1006 *Graphs, and Mathematical Tables.* Courier Corporation.
- 1007 ANDERSSON, P., BERGGREN, M. & HENNINGSON, D. S. 1999 Optimal disturbances and bypass  
1008 transition in boundary layers. *Phys. Fluids* **11** (1), 134–150.
- 1009 BAGHERI, S. & HANIFI, A. 2007 The stabilizing effect of streaks on Tollmien-Schlichting and  
1010 oblique waves: A parametric study. *Phys. Fluids* **19** (7), 078103.
- 1011 BROWN, S. N. 1985 Marginal separation of a three-dimensional boundary layer on a line of  
1012 symmetry. *J. Fluid Mech.* **158**, 95–111.
- 1013 COSSU, C. & BRANDT, L. 2002 Stabilization of Tollmien–Schlichting waves by finite amplitude  
1014 optimal streaks in the Blasius boundary layer. *Phys. Fluids* **14** (8), L57–L60.
- 1015 COSSU, C. & BRANDT, L. 2004 On Tollmien–Schlichting-like waves in streaky boundary layers.  
1016 *Eur. J. Mech. B/Fluids* **23** (6), 815–833.
- 1017 DENISSEN, N. A. & WHITE, E. B. 2013 Secondary instability of roughness-induced transient  
1018 growth. *Phys. Fluids* **25** (11), 114108.
- 1019 DOWNS, R. S. & FRANSSON, J. H. M. 2014 Tollmien–Schlichting wave growth over spanwise-  
1020 periodic surface patterns. *J. Fluid Mech.* **754**, 39–74.
- 1021 DUCK, P. W. & BURGGRAF, O. R. 1986 Spectral solutions for three-dimensional triple-deck  
1022 flow over surface topography. *J. Fluid Mech.* **162**, 1–22.
- 1023 FRANSSON, J. H. M., BRANDT, L., TALAMELLI, A. & COSSU, C. 2004 Experimental and  
1024 theoretical investigation of the nonmodal growth of steady streaks in a flat plate boundary  
1025 layer. *Phys. Fluids* **16** (10), 3627–3638.
- 1026 FRANSSON, J. H. M., BRANDT, L., TALAMELLI, A. & COSSU, C. 2005 Experimental study of  
1027 the stabilization of Tollmien–Schlichting waves by finite amplitude streaks. *Phys. Fluids*  
1028 **17** (5), 054110.
- 1029 FRANSSON, J. H. M. & TALAMELLI, A. 2012 On the generation of steady streamwise streaks  
1030 in flat-plate boundary layers. *J. Fluid Mech.* **698**, 211–234.
- 1031 FRANSSON, J. H. M., TALAMELLI, A., BRANDT, L. & COSSU, C. 2006 Delaying transition to  
1032 turbulence by a passive mechanism. *Phys. Rev. Lett.* **96** (6), 064501.
- 1033 GOLDSTEIN, M. E., SESCU, A., DUCK, P. W. & CHOUDHARI, M. 2016 Nonlinear wakes behind  
1034 a row of elongated roughness elements. *J. Fluid Mech.* **796**, 516–557.
- 1035 GOLDSTEIN, M. E., SESCU, A., DUCK, P. W. & CHOUDHARI, M. 2010 The long range  
1036 persistence of wakes behind a row of roughness elements. *J. Fluid Mech.* **644**, 123–163.
- 1037 GOVINDARAJAN, R. AND NARASIMHA, R. 1997 A low-order theory for stability of non-parallel  
1038 boundary layer flows. *Proc. R. Soc. Lond. A* **453** (1967), 2537–2549.
- 1039 GREEN, J. E. 2008 Laminar flow control – back to the future? *AIAA Paper* 2008-3738.
- 1040 GAD-EL HAK, M. 2000 *Transition Control*, p. 104–119. Cambridge University Press.
- 1041 HALL, P. & HORSEMAN, N. J. 1991 The linear inviscid secondary instability of longitudinal  
1042 vortex structures in boundary layers. *J. Fluid Mech.* **232**, 357–375.
- 1043 HALL, P. & SMITH, F. T. 1990 Near-planar TS waves and longitudinal vortices in channel flow:  
1044 nonlinear interaction and focussing. *Instability and transition*, pp. 5–39. Springer.
- 1045 HERBERT, T. 1988 Secondary instability of boundary layers. *Annu. Rev. Fluid Mech.* **20** (1),  
1046 487–526.
- 1047 JOSLIN, R. D. 1998 Aircraft laminar flow control. *Annu. Rev. Fluid Mech.* **30** (1), 1–29.
- 1048 KÁTAI, C. B. 2020 Asymptotic description of transitional and turbulent flows: effects of surface  
1049 roughness on the boundary layer and the evolution of coherent structures in free shear  
1050 flows. PhD thesis, Imperial College London.
- 1051 KLEBANOFF, P. S. & TIDSTROM, K. D. 1972 Mechanism by which a two-dimensional roughness  
1052 element induces boundary-layer transition. *Phys. Fluids* **15** (7), 1173–1188.
- 1053 LI, F. & MALIK, M. R. 1995 Fundamental and subharmonic secondary instabilities of Görtler  
1054 vortices. *J. Fluid Mech.* **297**, 77–100.
- 1055 LIN, C. C. 1945 On the stability of two-dimensional parallel flows. III. Stability in a viscous  
1056 fluid. *Quart. Appl. Math.* **3** (4), 277–301.
- 1057 LUCHINI, P. 2000 Reynolds-number-independent instability of the boundary layer over a flat  
1058 surface: optimal perturbations. *J. Fluid Mech.* **404**, 289–309.

- 1059 MESSITER, A. F. 1970 Boundary-layer flow near the trailing edge of a flat plate. *SIAM Journal*  
 1060 *on Applied Mathematics* **18** (1), 241–257.
- 1061 MULLER, D. E. 1956 A method for solving algebraic equations using an automatic computer.  
 1062 *Math. Tables and Aids to Comput.* **10** (56), 208–215.
- 1063 NAYFEH, A. H., RAGAB, S. A. & AL-MAAITAH, A. A. 1988 Effect of bulges on the stability of  
 1064 boundary layers. *Phys. Fluids* **31** (4), 796–806.
- 1065 NEILAND, V. Y. 1969 Theory of laminar boundary layer separation in supersonic flow. *Fluid*  
 1066 *Dynamics* **4** (4), 33–35.
- 1067 ORSZAG, S. A. 1971 On the elimination of aliasing in finite-difference schemes by filtering high-  
 1068 wavenumber components. *J. Atm. Sci.* **28** (6), 1074–1074.
- 1069 PIOT, E., CASALIS, G. & RIST, U. 2008 Stability of the laminar boundary layer flow  
 1070 encountering a row of roughness elements: Biglobal stability approach and DNS. *Eur.*  
 1071 *J. Mech. B/Fluids* **27** (6), 684–706.
- 1072 PRANDTL, L. 1938 Zur Berechnung der Grenzschichten. *Z. Angew. Math. Mech.* **18** (1), 77–82.
- 1073 REED, H. L. & NAYFEH, A. H. 1986 Numerical-perturbation technique for stability of flat-plate  
 1074 boundary layers with suction. *AIAA J.* **24** (2), 208–214.
- 1075 REYNOLDS, G. A. & SARIC, W. S. 1986 Experiments on the stability of the flat-plate boundary  
 1076 layer with suction. *AIAA J.* **24** (2), 202–207.
- 1077 RICCO, P., LUO, J. & WU, X. 2011 Evolution and instability of unsteady nonlinear streaks  
 1078 generated by free-stream vortical disturbances. *J. Fluid Mech.* **677**, 1–38.
- 1079 ROZHKO, S. B. & RUBAN, A. I. 1987 Longitudinal-transverse interaction in a three-dimensional  
 1080 boundary layer. *Fluid Dyn.* **22** (3), 362–371.
- 1081 ROZHKO, S. B., RUBAN, A. I. & TIMOSHIN, S. N. 1988 Interaction of a three-dimensional  
 1082 boundary layer with an extensive obstacle. *Fluid Dyn.* **23** (1), 30–37.
- 1083 RUBAN, A. I. 1982 Asymptotic theory of short separation regions on the leading edge of a  
 1084 slender airfoil. *Fluid Dynamics* **17** (1), 33–41.
- 1085 SARIC, W. S., REED, H. L. & KERSCHEN, E. J. 2002 Boundary-layer receptivity to freestream  
 1086 disturbances. *Annu. Rev. Fluid Mech.* **34** (1), 291–319.
- 1087 SATTARZADEH, S. S., FRANSSON, J. H. M., TALAMELLI, A. & FALLENIOUS, B. E. G. 2014  
 1088 Consecutive turbulence transition delay with reinforced passive control. *Phys. Rev. E*  
 1089 **89** (6), 061001.
- 1090 SHAHINFAR, S., FRANSSON, J. H. M., SATTARZADEH, S. S. & TALAMELLI, A. 2013 Scaling of  
 1091 streamwise boundary layer streaks and their ability to reduce skin-friction drag. *J. Fluid*  
 1092 *Mech.* **733**, 1–32.
- 1093 SHAHINFAR, S., SATTARZADEH, S. S. & FRANSSON, J. H. M. 2014 Passive boundary layer  
 1094 control of oblique disturbances by finite-amplitude streaks. *J. Fluid Mech.* **749**, 1–36.
- 1095 SHAHINFAR, S., SATTARZADEH, S. S., FRANSSON, J. H. M. & TALAMELLI, A. 2012 Revival of  
 1096 classical vortex generators now for transition delay. *Phys. Rev. Lett.* **109** (7), 074501.
- 1097 SICONOLFI, L., CAMARRI, S. & FRANSSON, J. H. M. 2015 Stability analysis of boundary layers  
 1098 controlled by miniature vortex generators. *J. Fluid Mech.* **784**, 596–618.
- 1099 SMITH, F. T. 1979*a* Instability of flow through pipes of general cross-section. Part 1.  
 1100 *Mathematika* **26** (2), 187–210.
- 1101 SMITH, F. T. 1979*b* On the non-parallel flow stability of the Blasius boundary layer. *Proc. R.*  
 1102 *Soc. Lond. A* **366**, 91–109.
- 1103 SMITH, F. T., BRIGHTON, P. W. M., JACKSON, P. S. & HUNT, J. C. R. 1981 On boundary-  
 1104 layer flow past two-dimensional obstacles. *J. Fluid Mech.* **113**, 123–152.
- 1105 SMITH, F. T., SYKES, R. I. & BRIGHTON, P. W. M. 1977 A two-dimensional boundary layer  
 1106 encountering a three-dimensional hump. *J. Fluid Mech.* **83** (1), 163–176.
- 1107 STEWARTSON, K. & SIMPSON, C. J. 1982 On a singularity initiating a boundary-layer collision.  
 1108 *Q. J. Mech. Appl. Maths* **35** (1), 1–16.
- 1109 STEWARTSON, K., SMITH, F. T. & KAUPS, K. 1982 Marginal separation. *Stud. Appl. Maths*  
 1110 **67** (1), 45–61.
- 1111 STEWARTSON, K. & WILLIAMS, P. G. 1969 Self-induced separation. *Proc. R. Soc. Lond. A*, ,  
 1112 vol. 312, pp. 181–206. The Royal Society.
- 1113 THEOFILIS, V. 2011 Global linear instability. *Annu. Rev. Fluid Mech.* **43**, 319–352.
- 1114 VAN DYKE, M. 1975 *Perturbation methods in fluid mechanics*. The Parabolic Press.
- 1115 WALSH, M. J. 1982 Turbulent boundary layer drag reduction using riblets. *AIAA Paper* 82-0169.

- 1116 WALTON, A. G. 1996 Strongly nonlinear vortex–Tollmien–Schlichting–wave interactions in the  
1117 developing flow through a circular pipe. *J. Fluid Mech.* **319**, 77–107.
- 1118 WALTON, A. G. & PATEL, R. A. 1998 On the neutral stability of spanwise-periodic boundary-  
1119 layer and triple-deck flows. *Q. J. Mech. Appl. Math.* **51** (2), 311–328.
- 1120 WHITE, E. B. 2002 Transient growth of stationary disturbances in a flat plate boundary layer.  
1121 *Phys. Fluids* **14** (12), 4429–4439.
- 1122 WU, X. & DONG, M. 2016 A local scattering theory for the effects of isolated roughness on  
1123 boundary-layer instability and transition: transmission coefficient as an eigenvalue. *J.*  
1124 *Fluid Mech.* **794**, 68–108.
- 1125 WU, X. & HOGG, L. W. 2006 Acoustic radiation of Tollmien–Schlichting waves as they undergo  
1126 rapid distortion. *J. Fluid Mech.* **550**, 307–347.
- 1127 XU, H., LOMBARD, J.-E. W. & SHERWIN, S. J. 2017*a* Influence of localised smooth steps on  
1128 the instability of a boundary layer. *J. Fluid Mech.* **817**, 138–170.
- 1129 XU, H., MUGHAL, S. M., GOWREE, E. R., ATKIN, C. J. & SHERWIN, S. J. 2017*b* Destabilisation  
1130 and modification of Tollmien–Schlichting disturbances by a three-dimensional surface  
1131 indentation. *J. Fluid Mech.* **819**, 592–620.
- 1132 XU, H., SHERWIN, S. J., HALL, P. & WU, X. 2016 The behaviour of Tollmien–Schlichting  
1133 waves undergoing small-scale localised distortions. *J. Fluid Mech.* **792**, 499–525.